

1 **Small-Scale Structure of the Mid-Latitude Storm**  
2 **Enhanced Density Plume During the March 17, 2015**  
3 **St. Patrick's Day Storm**

Thomas R.P. Heine,<sup>1</sup> Mark B. Moldwin,<sup>1</sup> and Shasha Zou<sup>1</sup>

---

<sup>1</sup>Department of Climate and Space  
Sciences and Engineering, University of  
Michigan, Ann Arbor, Michigan, USA.

This is the author manuscript accepted for publication and has undergone full peer review but has not been through the copyediting, typesetting, pagination and proofreading process, which may lead to differences between this version and the Version of Record. Please cite this article as doi:10.1002/2016JA022963

D R A F T  
March 11, 2017, 1:12pm

D R A F T

**Key Points.**

- Irregularity length scales are determined from single GPS station total electron content.
- Kilometer scale irregularities were detected along the poleward edge of the storm enhanced density plume and into the trough.
- Kilometer scale irregularities were not detected on the equatorward gradient or within the storm enhanced density plume.

**Abstract.**

Kilometer-scale density irregularities in the ionosphere can cause ionospheric scintillation — a phenomenon that degrades space-based navigation and communication signals. During strong geomagnetic storms, the mid-latitude ionosphere is primed to produce these  $\sim 1\text{-}10$  km small-scale irregularities along the steep gradients between mid-latitude storm enhanced density (SED) plumes and the adjacent low-density trough. The length scales of irregularities on the order of 1-10 km are determined from a combination of spatial, temporal, and frequency analyses using single-station ground based Global Positioning System Total Electron Content (TEC) combined with radar ion velocity measurements. Kilometer-scale irregularities are detected along the boundaries of the SED plume and depleted density trough during the 17 March 2015 geomagnetic storm, but not equatorward of the plume or within the plume itself. Analysis using the Fast Fourier Transform (FFT) of high pass filtered slant TEC suggests that the kilometer-scale irregularities formed near the poleward gradients of SED plumes can have similar, intensity and length

20 scales to those typically found in the aurora, but are shown to be distinct  
21 phenomena in spacecraft electron precipitation measurements.

Author Manuscript

D R A F T

March 11, 2017, 1:12pm

D R A F T

## 1. Introduction

22 The small-scale ( $\sim 1$ -10 km) density structure of the storm-time, mid-latitude ionosphere  
23 is a crucial observation in understanding the space weather effects on key space-based in-  
24 frastructure and especially communication and navigation systems. Though these systems  
25 are generally unaffected by the mid-latitude ionosphere, there can be significant techno-  
26 logical impacts during strong geomagnetic storms. Geomagnetic storms have been shown  
27 to drive structural changes in the Earth's ionosphere that deviate dramatically from the  
28 typical quiet-time conditions [e.g., *Foster and Rideout*, 2005]. Observations of Total Elec-  
29 tron Content (TEC) have revealed that some of the most dramatic changes are the SED  
30 plumes that occur in the mid-latitude ionosphere [e.g., *Foster*, 1993; *Kelley et al.*, 2004;  
31 *Zou et al.*, 2013, 2014]. Storm Enhanced Density (SED) plumes and the sub-auroral po-  
32 larization stream (SAPS) can generate radio-disrupting ionospheric density irregularities  
33 [*Foster and Burke*, 2002; *Basu et al.*, 2008] that produce up to 20 dB signal fade at the  
34 Global Positioning System (GPS) L1 (1575 MHz) frequency and scintillations in HF and  
35 VHF communications [*Basu and Groves*, 2001; *Ledvina et al.*, 2002; *Seo et al.*, 2011]. Steep  
36 density gradients along the plumes' edges can produce a cascade of small-scale density ir-  
37 regularities and subsequently, a potentially worsening scintillation environment for Global  
38 Navigation Satellite Systems (GNSS) such as GPS, and space-based communication users.  
39 Small-scale variations (or irregularities) in ionospheric electron density corresponding to  
40 the Fresnel radius of radio frequencies — between 100 MHz - 3 GHz for a receiver on the  
41 ground — can have dramatic impacts on space-based systems operating in this frequency  
42 range [*Datta-Barua et al.*, 2014; *Doherty et al.*, 2004; *Datta-Barua et al.*, 2003].

43 This paper will demonstrate, through a case study into the geomagnetic storm of 17  
44 March 2015, a proof-of-concept for the detection and characterization of small-scale ( $\sim$ 1-  
45 10 km) irregularities from a single GPS TEC station (located in Ann Arbor, Michigan —  
46  $42.29^\circ$  N,  $-83.71^\circ$  E Geodetic,  $53.31^\circ$  N,  $-10.34^\circ$  E CGM). When combined with coherent  
47 high frequency (HF) and incoherent scatter radar (ISR) ion velocities, the irregularity  
48 length scales can be inferred. Further, using publicly available TEC maps from the MIT  
49 Madrigal Archival Database to plot the location of the single station TEC measurements  
50 places these observations in context of the broader SED plume background system. These  
51 are the first observations of mid-latitude kilometer-scale irregularities during a SED event  
52 to identify length scales from single-station GPS TEC.

### 1.1. Background

53 The origins of kilometer-scale irregularities at mid-latitudes owe to three potential  
54 sources. In the first, spatially structured and temporally variable particle precipitation  
55 produces localized small-scale structure in the E and F regions of the auroral zone. [*Schunk*  
56 *and Nagy*, 2009]. In the second, it has been suggested that small-scale irregularities are  
57 generated near the SED plume by a horizontal Rayleigh-Taylor instability (also known as  
58 the gradient drift instability) caused by the motion of lower density plasma moving into the  
59 density gradient. This condition becomes unstable when  $(\mathbf{E} \times \mathbf{B}) \cdot \nabla n > 0$  [*Simon*, 1963;  
60 *Sun et al.*, 2013]. Finally, in the third, velocity shear instability (Kelvin-Helmholtz) may  
61 play a role in generating small-scale irregularities at the interface between fluids of differ-  
62 ent densities [*Hargreaves*, 1992], such as in the case of the SED/SAPS boundary. Although  
63 the physics underpinning the formation of small-scale irregularities is well understood, the  
64 complexity of the storm-time mid-latitude ionosphere demands further observation and

65 characterization of its density structure at all scales to improve our understanding of the  
66 typical formation and evolution of storm-time small-scale irregularities and the potential  
67 for mid-latitude radio scintillation. This paper describes a method for detecting small-  
68 scale density irregularities using spectral analysis (Fast Fourier Transform) of GPS TEC  
69 observations from a single ground station. While simultaneously “zooming-out” to see  
70 the location of the single station measurements in the broader (1000 km) context of the  
71 SED plume system.

72 Mid-latitude irregularities and scintillation have been a subject of study for several  
73 decades. An early investigation by *Bramley and Browning* [1978], over a twelve-month  
74 period, analyzed the spectral composition of VHF scintillation near Slough, in Berkshire,  
75 England (48.4° N and 79.3° E CGM). Using spaced, arial antennas to measure amplitude  
76 fluctuations from the interaction between a geostationary satellite signal and ionospheric  
77 irregularities. They were able to infer both the irregularity size and approximate orienta-  
78 tion from the ground diffraction pattern. The irregularities they observed had character-  
79 istic spatial scales ranging from 180 m to 2 km and found no correlation of the occurrence  
80 of these irregularities with geomagnetic activity — suggesting their observations were not  
81 of storm related effects.

82 The stormtime effects of SED have been extensively described in the literature over  
83 the past decade. *Doherty et al.* [2004] established a connection between SED gradients  
84 and disruption of the Federal Aviation Administration’s (FAA) Wide-Area Augmentation  
85 System (WAAS) during the October/November 2003 “Halloween Storms”. During those  
86 events, the WAAS vertical navigation (VNAV) system was inoperable for more than 28  
87 hours over a two day period. Similarly, *Basu et al.* [2008] looked at a geomagnetic storm

88 7-8 November 2004 with a minimum Kyoto Disturbance Storm Time index (Dst) of -394  
89 nT. They observed mid-latitude GNSS disruption due to irregularities from an expanding  
90 auroral oval and nighttime sub-auroral polarization stream (SAPS) flow. *Datta-Barua*  
91 *et al.* [2014] also described the the impact on the WAAS during 24-25 October 2011  
92 and 9 October 2012 geomagnetic storms that included reduced service coverage over the  
93 continental United States lasting several hours and anomalous receiver tracking due to  
94 ionospheric scintillation.

95 *Coster* [2007] first reported the impact of TEC variability on the performance of key  
96 infrastructure, including WAAS, and specifically the impact of TEC gradients. Using  
97 observations of GPS tracks crossing SED plumes, *Coster* [2007] observed the TEC gra-  
98 dients near SED plumes can exhibit differing degrees of variability and even between the  
99 poleward and equatorward gradients. The nature and specific irregularity length scales of  
100 such crossings remains an open research area.

101 Another study by *Sun et al.* [2013] analyzed the formation of irregularities associated  
102 with North American SED plumes during geomagnetic storms on 31 March 2001 (Dst = -  
103 387 nT) and 30 October 2003 (Dst = -383 nT). In their study, the presence of irregularities  
104 was indicated in TEC maps with  $0.5^\circ \times 1.0^\circ$  resolution using a 30 s rate of TEC (ROT)  
105 and the ROT index (ROTI) formulated by *Pi et al.* [1997] at each grid point. ROT and  
106 ROTI are defined as the differential vertical TEC (VTEC) between time steps converted  
107 to TEC units per minute (TECU/min), where a TECU =  $1 \times 10^{16}$  electrons  $\text{m}^{-2}$ , and the  
108 standard deviation of the ROT over a specified time interval — commonly 5 minutes. *Sun*  
109 *et al.* [2013] observed that irregularities were most present along the poleward boundary of  
110 the SED — along the low density trough — and that the irregularity intensity increased

111 with steepening TEC gradients in some cases. They concluded that the formation of  
112 irregularities appeared to depend on both steep TEC gradients and strong ion drifts  
113 ( $1\text{-}2\text{ km s}^{-1}$ ) as favorable conditions. However, while they identified the presence of  
114 irregularities and the gradients associated with ROTI, they did not specify the length-  
115 scale of irregularities present in each grid cell.

116 Previously, characteristic sizes of mid-latitude small-scale irregularities associated with  
117 SED plumes have been inferred from amplitude scintillation measurements at a fixed  
118 point [*Basu et al.*, 2008] and *van der Meeren et al.* [2014] used similar methodology to  
119 that presented here to identify irregularities in 50 Hz GPS phase data detrended with  
120 fourth-order polynomial fit and a high-pass Butterworth filter to investigate irregularities  
121 at the front of a polar tongue of ionization on 31 October 2011. They found phase  
122 variations at spatial scales from 100 m to 5 km using spectrograms and estimates of TOI  
123 drift speed from arrival time of the Tongue of Ionization at two European Incoherent  
124 Scatter (EISCAT) Radar antennae.

125 To date, there have been no such studies inferring the spatial scale of kilometer-scale  
126 irregularities associated with mid-latitude SED plumes from single station GPS TEC  
127 using multiple GPS IPPs in an SED plume system. This paper describes the detection  
128 and length-scale estimation of irregularities associated with the mid-latitude SED plume  
129 as it moves over the GPS receiver during the 17 March 2015 geomagnetic storm.

## 1.2. The 2015 St. Patrick's Day Storm

130 On 17 March 2015, the Earth experienced a G4 “severe” geomagnetic storm on the Na-  
131 tional Oceanic and Atmospheric Administration (NOAA) geomagnetic storm scale [*Love*  
132 *and Rigler*, 2015]. At 04:45 UTC, the Kyoto Dst indicated a 55 nT enhancement of the



133 horizontal geomagnetic field which is characteristic of a sudden storm commencement.  
134 The storm reached the peak of its main phase around 19:00 UTC with minimum mag-  
135 netic field disturbances: Kyoto Provisional Dst = -223 nT and Sym H = -234 nT. Over  
136 the period between 16 March 2015 and 19 March 2015, the NOAA Planetary K-index  
137 ( $K_p$ ) was greater than 5 for 48 of 72 hours and  $K_p = 8$  for a total of 9 hours during the  
138 main phase of the storm. Meanwhile, throughout 17 and 18 March, the NOAA reported  
139 K-index reached  $K_p \geq 7$  on four of twenty-four 3-hour periods and above 5 during sixteen  
140 periods. A SED plume was observed in the MIT Madrigal TEC map during the North  
141 American afternoon/dusk period on 17 March (shown in Figure 1). The SED plume be-  
142 gan in a region of enhanced TEC (the SED base) that was poleward and distinct from the  
143 TEC peaks of the enhanced equatorial anomaly. The plume extended to the northwest  
144 across the Great Lakes region and toward the noontime cusp. A low-density, mid-latitude  
145 trough is also visible in Figure 1, while the auroral oval extended as far south as 39°  
146 geographic latitude at 23:17 UT (inferred from Figure 6 and discussed in section 3.5).  
147 The Dst minimum was reached at approximately 23:00 UT. This paper includes obser-  
148 vations from a single GPS station in Ann Arbor, Michigan: ANNA (42.29 N, -83.71 E  
149 Geodetic; 53.31 N, -10.34 E CGM), during the end of the main phase and the beginning  
150 of the recovery phase between 20:00 UT 17 March 2015 and 23:57 UT 18 March 2015.  
151 The availability of high rate (1 Hz) TEC is rare within this region for this time. Of  
152 the few stations within 250 km of Ann Arbor that have 1 Hz data available during this  
153 event, two Canadian stations, ALGO (45.96 N -78.07 E GEO, 56.74 N -2.57 E CGM) and  
154 NRC1 (45.454 N -75.62 E GEO, 56.04 N 0.97 E CGM), do have 1 Hz data for this time,  
155 but are too high in latitude and too far ahead in local time relative to the SED plume

156 to distinguish between auroral precipitation and plume generated irregularities and are  
157 therefore not used. Within 1000 km, there are six stations in the UNAVCO database with  
158 1 Hz data rates. Stations in Ames, IA (AMES: 41.98 N -93.68 E GEO, 52.58 N -25.37  
159 E CGM) and near St. Clairsville, PA (P817: 40.14 N -78.51 E GEO, 52.59 N -3.51 E  
160 CGM) were analyzed using the the same methods described in Section 2 of this paper  
161 and produce similar results to the data observed at ANNA in terms of general trend, but  
162 being 900 km west and 700 km east of ANNA respectively, they exhibit the expected  
163 localized differences in density structure  $>10$  km. This suggests that for the purpose of  
164 this study, ANNA is representative of the available 1 Hz GPS TEC data for this event.

## 2. Methodology

165 Kilometer-scale irregularities are identified near the SED plume using multiple line-of-  
166 sight GPS TEC measurements from a single GPS receiver. Slant TEC (STEC) from each  
167 GPS satellite/receiver pair was measured at 1 Hz using a Trimble NetR9 dual-frequency  
168 GPS receiver, and pseudo random noise (PRN) codes — assigned 1-32 to each of the cur-  
169 rently operational GPS spacecraft — are used to identify individual satellites and their  
170 associated Ionospheric Pierce Points (IPP). IPP are defined as the point of intersection  
171 between a GPS signal path and the altitude of the ionospheric F-peak, which is approxi-  
172 mated as a spherical shell at 300 km altitude. TEC is derived from the differential (GPS  
173 L1 and L2 frequencies) P-code pseudorange and the carrier phase. The two-frequency dif-  
174 ferential carrier phase measurement allows precise measurement of the carrier phase delay  
175 while the PRN code pseudorange is used to resolve the cycle ambiguity inherent to the  
176 carrier phase measurements. The STEC is converted to the local vertical TEC (VTEC)  
177 at the IPP using a spherical mapping function. A post-processing elevation mask of  $20^\circ$

178 is applied to reduce errors from the vertical mapping function and obstructions near the  
179 horizon. The STEC data are then filtered using a tenth-order Butterworth high pass  
180 filter shaped with stop and pass frequencies at 30 and 100 mHz respectively. The filter's  
181 frequency and forward phase response are shown in the top panel of Figure 2. The filter  
182 is designed to suppress the low-frequency background density structure in STEC while  
183 maintaining higher frequency power from smaller fluctuations. It is also designed to min-  
184 imize phase shifts and the filter function was convolved with the data both forward and  
185 backward to further cancel phase changes to the filtered signal. The unfiltered and filtered  
186 STEC are shown in the bottom panel of Figure 2.

187 The Discrete (Fast) Fourier Transform (FFT) of the filtered STEC for each PRN was  
188 computed in a sliding five-minute window advanced in ten seconds increments. The  
189 sliding five-minute window (300 samples, 290 overlap) was chosen as a balance between  
190 three factors: first, to achieve a sufficient number of samples to resolve spectra with a  
191 resolution of at least 0.1 Hz; second, to maintain a sufficiently short IPP track ( $\sim 15$  km)  
192 so that the resulting spectra can be attributed to a specific location within the SED plume  
193 system (e.g. a gradient crossing) and third, to take advantage of the maximum temporal  
194 resolution available from the TEC maps which are updated every five minutes.

195 Additionally, to ensure a consistent number of samples between PRN in each FFT in-  
196 terval, measurements of PRN that were visible less than 90% of the interval were excluded  
197 from analysis.

198 Finally, by combining the FFT spectra with the radar velocity measurements, including  
199 those shown in Figure 1, the length-scales of small-scale variability can be estimated.  
200 Millstone Hill radar measures the ion drift velocity during azimuthal scans looking at  $6^\circ$

201 elevation toward the west and observes the ionosphere at a height of  $\sim 300$  km above the  
202 Ann Arbor viewing area. Several mid-latitude SuperDARN radars (Blackstone, Christmas  
203 Valley East, Fort Hays East, and Wallops Island) also measure ion velocity in this region.  
204 If it is assumed that irregularities are frozen-in with the background plasma flow (as  
205 has been suggested by [e.g., *Yeh and Liu, 1982*]), and the IPP velocity  $v_{ipp} \ll v_{ion}$ ,  
206 ( $v_{ipp} \sim 50$  m s $^{-1}$ ), then the FFT power at various frequencies can reasonably be attributed  
207 to irregularities of certain length scales being transported past the relatively stationary  
208 IPP at the ion velocity. Consider the simplified scenario: discrete and uniformly-spaced  
209 boxcar irregularities passing a nearly stationary IPP produce a periodicity in the slant  
210 TEC data that is revealed in the FFT frequency domain. Therefore, if the irregularity  
211 velocity is known (which is assumed to be with the background ion velocity), then the  
212 irregularity length-scale can be estimated by  $L_{irr} \approx v_{ion}/f_{FFT}$ . Uncertainty introduced  
213 by the IPP velocity contributes only at most a shift in the frequency spectra of  $\sim 0.005$   
214 Hz within the 0 - 0.5 Hz Nyquist window.

215 Unlike methods that measure signal amplitude to detect ionospheric variability and  
216 scintillation at that signal frequency, this method can be used to detect irregularities of  
217 multiple length-scales and is limited only by the TEC sample rate. The case presented  
218 here uses TEC sampled at 1 Hz. Future studies will extend this approach to sample rates  
219 of 20 Hz and higher to include smaller length scales and expand to include multiple GPS  
220 TEC stations.

221 The single station TEC measurements and analysis are put compared and contextual-  
222 ized in the broader SED plume system using multi-station GPS TEC maps downloaded  
223 from the MIT Madrigal archival site at Millstone Hill, MA. The location of the Ann Ar-

224 bor station IPP tracks are then superimposed on the MIT Madrigal TEC map. The MIT  
225 Madrigal Database provides global maps of TEC on a  $1^\circ \times 1^\circ$  spatial grid updated every  
226 five minutes. The maps are fitted to a  $1/6^\circ \times 1/6^\circ$  subgrid mesh using bi-cubic spline  
227 interpolation — a common image sharpening technique. The interpolated map clarifies  
228 the locations and boundaries of the SED plume, through, and auroral enhancement so  
229 that the location of the IPPs from the single-station data can be plotted on the map and  
230 categorized by their location within the SED plume system. However, since interpolation  
231 cannot add information, the location of structural dimensions appearing less than a degree  
232 in scale, such as the plume boundary's thickness, is uncertain using the TEC map data  
233 alone, however TEC structures with dimensions larger than a degree (e.g. the line of the  
234 plume boundary,  $10\text{-}20^\circ$  lon. in scale), are reliably defined using this technique. Definitive  
235 boundary crossings of each IPP are confirmed using the direct measurement Ann Arbor  
236 single station TEC time series.

237 While the Madrigal TEC maps provide the background density structure spatial scales  
238 on the order of the SED plume system (100-1000 km), the Ann Arbor STEC data provide  
239 measurements a of the density structure on much smaller ( $<100$  km) spatial and temporal  
240 scales. GPS IPP tracks for the Ann Arbor receiver are calculated from the precise GPS  
241 satellite ephemeris, provided by the International GNSS Service (IGS) and the NASA Jet  
242 Propulsion Laboratory (JPL) in Standard Product-3 (.SP3) format, and are superimposed  
243 onto the TEC maps to illustrate where the small-scale STEC measurements were made  
244 relative to the background SED plume density structure.

245 One of the interesting, and perhaps counter-intuitive, aspects of the Earth-fixed TEC  
246 maps is the apparent southwestward motion of the SED plume through the observation

247 area. This is due to two factors: 1) at mid-latitudes, the SED plume is connected to the  
248 plasmaspheric convection flow and does not co-rotate with the Earth. A consequence of  
249 this is that, in the Earth-fixed inertial frame, the Earth rotates underneath the plume  
250 — giving the impression of a westward moving plume. 2) the plasma within the plume  
251 is convecting to the northwest from a broader base region and is angled relative to the  
252 Earth's eastward rotation. This means that what appears in figures to be a southward  
253 component in the motion of the plume is actually due to the Earth rotating under a  
254 broader region of the plume near the SED base region.

255 An animation (Dynamic Figure 1) encompassing the period from 20:00 UT to 23:57  
256 UT 17 March 2015 to combines single station VTEC time series, sliding FFT, and MIT  
257 Madrigal TEC maps into three panes. Each of the animation's three panes are synchro-  
258 nized with the five-minute TEC map update and IPP track. Since the IPP move at about  
259  $50 \text{ m s}^{-1}$ , a five-minute window covers  $\sim 15 \text{ km}$  and the IPP tracks appear as short line  
260 segments overlaid in the mapping pane. The VTEC time series and FFT are updated  
261 more frequently — corresponding to the ten-second sliding FFT window. A gray vertical  
262 bar superimposed on the VTEC time series illustrates the period of the FFT interval.  
263 Meanwhile, the Madrigal TEC map is updated when the leading edge of the FFT win-  
264 dow is at the mid-point between five-minute map update intervals. This ensures that the  
265 displayed map best represents the background against which the single station TEC FFT  
266 was computed.

267 In addition to GPS TEC observations, observations from the Defense Meteorological  
268 Satellite Program (DMSP) and the Active Magnetosphere and Planetary Electrodynam-  
269 ics Response Experiment (AMPERE) are used to locate regions of auroral precipitation.

270 DMSP measures vertical electron and ion fluxes while AMPERE estimates the hemi-  
271 spherical polar radial field-aligned current density derived from reduced magnetic field  
272 perturbation data from the Iridium satellite constellation. The DMSP and AMPERE ob-  
273 servations are used here to estimate the location of the auroral oval's equatorward bound-  
274 ary in order to delineate between the density irregularities and enhancements caused by  
275 aurora and those associated with the SED plume.

### 3. Observations

276 The SED plume is clearly visible from VTEC data in the observation area beginning  
277 around 20:00 UT. Figures 3-6 show results from key intervals, 20:40, 22:00 23:00, and  
278 23:20 UT, during the SED plume's passage over the Ann Arbor observation area. Each of  
279 these figures contains: *Left*: the track of IPPs in relation to the SED plume, *Right Top*:  
280 the VTEC time series, and *Right Bottom*: the 5-minute STEC FFT. Observations for the  
281 entire period of 20:00 UT 17 March 2015 to 00:00 UT 18 March 2015 are contained in the  
282 supplemental animation.

#### 3.1. 20:00 to 20:45 UT, Entering the SED Plume

283 During the period from 20:00 to 20:45 UT, the SED plume's equatorward edge and  
284 density peak passed over Ann Arbor (Figure 3). Overall, VTEC measurements from  
285 PRN IPPs that tracked equatorward of the SED plume were comparable to quiet time  
286 levels, and those that tracked near or inside the plume showed VTEC that was elevated  
287 above quiet time levels with minimal increased variability seen in the VTEC time series.  
288 For example, PRN 3, shown in bright green in Figure 3, has an IPP that remained ahead  
289 of the plume's advancing equatorward edge and showed smooth and relatively constant

290 VTEC values with little FFT power above 100 mHz. By contrast PRN 16 (purple), which  
291 tracked poleward into the plume, showed smooth, but increasing VTEC. Around 20:37,  
292 as it traveled  $> 1^\circ$  equatorward of the plume's equatorward edge, PRN 3 exhibited an  
293 increase in FFT power just above 100 mHz, though there were no variations observed at  
294 other frequencies or in the VTEC times series. PRN 23 (light blue) and PRN 31 (black)  
295 were first observed inside the plume and near its equatorward edge (not shown). PRN  
296 23 was located in the narrower, westward portion of the plume at  $-86^\circ$  E, while PRN 31  
297 was located to the east (near  $-81^\circ$  E) and closer to the SED base region. Both exhibited  
298 elevated VTEC, although PRN 23 was initially  $\sim 7$  TECU lower than PRN 31. Between  
299 20:00 and 20:45, the plume moved so that both PRN 23 and 31 were tracking across the  
300 plume. PRN 23 VTEC increased steadily, though with persistent small-scale variations  
301 and a slight increase in FFT power just above the noise floor at  $\sim 0.005 \text{ TECU}^2 \text{ Hz}^{-1}$  near  
302 100 mHz at 20:20 UT — corresponding to its crossing into a large-scale bite-out in VTEC  
303 along the SED plume's poleward edge. PRN 31 VTEC held at a consistent 26-27 TECU  
304 and exhibited small variations in the VTEC time series, but these did not significantly  
305 affect the FFT power spectra ( $< 0.005 \text{ TECU}^2 \text{ Hz}^{-1}$ ). PRN 31 also tracked between some  
306 of the plume's  $1\text{-}2^\circ$  lon. high density structures visible in the VTEC map — suggesting a  
307 possible explanation for its near constant VTEC.

### 3.2. 20:45 to 21:20 UT, Longitudinal Asymmetries and Inside the Plume

308 At 20:45, the plume crossed the PRN 9 IPP which tracked parallel to the plume's  
309 poleward edge. It registered an increase of 5 TECU accompanied by a slight increase  
310 in FFT power just above  $0.005 \text{ TECU}^2 \text{ Hz}^{-1}$  around 100 mHz upon entering the plume  
311 before it was again crossed by the plume's poleward edge, when it recorded a drop in



312 VTEC of  $\sim 15$  TECU and exhibited rapid fluctuations in VTEC of  $\sim 3$ -5 TECU with  
313 periods of 5-10 minutes through the decrease. These decreases were accompanied by FFT  
314 power of  $0.04 \text{ TECU}^2 \text{ Hz}^{-1}$  between 100 and 300 mHz. PRN 31 was observed along a  
315 similar path along the plume's poleward edge, though further east — near  $-80^\circ$  E. VTEC  
316 for PRN 31 was 5 TECU less than PRN 9, but registered a comparable decrease in VTEC  
317 after crossing the plume's edge. However, in contrast with PRN 19, the decrease exhibited  
318 smooth fluctuations over distances of  $\sim 30$  km, which were accompanied by a broadband  
319 increase in FFT power that continued until PRN 31 left the observation area at 21:25 UT.  
320 Meanwhile, PRN 16 and 23 both showed increased VTEC as they moved through the SED  
321 plume. PRN 23 initially continued its track inside the plume along its length, from  $-87^\circ$  to  
322  $-85^\circ$  E and near the poleward edge. It crossed the poleward edge around 21:00 and the arc  
323 of its IPP track continued a southward turn that followed behind the plume's advancing  
324 poleward edge. This afforded sustained observations of the plume's poleward boundary  
325 which exhibited large undulations in VTEC of  $\sim 10$  TECU over periods of approximately  
326 ten minutes accompanied by FFT power up to  $0.03 \text{ TECU}^2 \text{ Hz}^{-1}$ . PRN 16 continued  
327 tracking northward through the plume and toward the the poleward edge near  $-80^\circ$  E.  
328 Instead of small-scale variations observed in PRN 23 as it crossed the plume, PRN 16  
329 exhibited only smooth increases in VTEC with large-scale variations of 1-3 TECU over  
330  $\sim 10$  km were observed, similar to PRN 23, with no observable change in FFT power until  
331 21:23 when it crossed the poleward edge and recorded drops in VTEC of 10 TECU over  
332 five minutes and FFT power up to  $0.06 \text{ TECU}^2 \text{ Hz}^{-1}$  up to 0.2 Hz.

### 3.3. 21:30 to 22:50 UT, Entering the Mid-latitude Trough

333 Around 21:30, the plume's poleward edge passed over the observation area and PRN  
334 9,16, 23, and 31 showed sudden increases in FFT power while near the plume's poleward  
335 edge — PRN 23 especially showed a large increase in FFT power  $>0.1 \text{ TECU}^2 \text{ Hz}^{-1}$   
336 between 100 mHz and 300 mHz during 21:50-22:00 UT (Figure 4). During this interval,  
337 PRN 7 (dark green), 9 (brown), and 16 (purple) were inside the low-density trough and  
338 also exhibited increased FFT power of  $\sim 0.03\text{-}0.05 \text{ TECU}^2 \text{ Hz}^{-1}$ . PRN 19 and 27 were  
339 located entirely within the SED plume with no observable FFT power above  $0.005 \text{ TECU}^2$   
340  $\text{Hz}^{-1}$ . At 22:30 UT PRN 7 and 9 were in the vicinity of a gradient between the  
341 trough and the trough minimum and, unlike the other PRN observed at this time, showed  
342 a small increase in FFT power  $>0.05 \text{ TECU}^2 \text{ Hz}^{-1}$  beginning at  $\sim 80 \text{ mHz}$  and extending  
343 as high as 300 mHz. PRN 16, 19, 23, and 27 were also within the trough — though  
344 either well inside the trough minimum or far away from its edge gradients and showed no  
345 increase in FFT power  $>0.005 \text{ TECU}^2 \text{ Hz}^{-1}$ .

### 3.4. 22:50 to 23:30, The Mid-latitude Trough

346 Figure 5 shows the interval between 22:50 and 23:00 UT. Most of the observable PRN  
347 were located within the trough and away from density gradients near the SED plume or  
348 low-density trough minimum. VTEC values leveled off between 10 and 15 TECU and there  
349 were only minor changes in FFT power ( $\sim 0.01 \text{ TECU}^2 \text{ Hz}^{-1}$ ) — mostly associated with  
350 PRN 9 and 16, which were approaching the observed VTEC enhancement of the auroral  
351 oval. PRN 23 (light blue) was the closest to the SED plume and headed equatorward,  
352 though still lagging behind the SED plume's poleward edge. It recorded increasing VTEC  
353 as the plume's poleward gradient crossed over it, but no FFT power was observed. PRN

354 19 (black) traversed a similar portion of the plume during this time, but moving poleward,  
355 and showed a steady and smooth, but slightly steeper decrease in density away from the  
356 plume with no FFT power changes. PRN 9 (brown) and 27 (blue) were near the trough  
357 region and showed a difference of  $\sim 2$  TECU between the trough's poleward gradient  
358 (PRN 9) and its base (PRN 27) and their FFT spectra do not show any obvious small-  
359 scale variations. Meanwhile, PRN 7 (dark green) and 16 (purple) were on the poleward  
360 edge of the trough, near the positive gradient into a region of auroral density enhancement.  
361 Both IPP time series showed low VTEC (10-15 TECU), with a slight increase of  $\sim 0.01$   
362  $\text{TECU}^2 \text{ Hz}^{-1}$  in the FFT power for PRN 7 — likely due small-scale structure in the auroral  
363 enhancement.

364 Figure 6 shows the interval between 23:10 and 23:20 UT. Shortly after the period shown  
365 in Figure 5, PRN 23 continued to track just poleward of the SED plume and showed a  
366 slight decrease in VTEC with some increased FFT power of  $0.02 \text{ TECU}^2 \text{ Hz}^{-1}$  near 100  
367 mHz. PRN 19, which had previously been parallel to PRN 23, continued its poleward  
368 track and traversed the low-density trough around 23:10 UT and measuring VTEC  $\sim 5$   
369 TECU accompanied by FFT power of  $0.03 \text{ TECU}^2 \text{ Hz}^{-1}$  at 100 mHz. PRN 9, 16, and  
370 27 continued to track poleward and crossed into the region of auroral enhancement and  
371 showed the expected increase in VTEC and strongly increased FFT power on a band  
372 around  $\sim 100$  mHz and extending to 350 mHz (in the case of PRN 7). PRN 7 and 30  
373 (violet) traverse the edges of the densest regions of the auroral enhancement. They showed  
374 the expected increase in VTEC from auroral ionization and also a strong increase in FFT  
375 power ( $> 0.1 \text{ TECU}^2 \text{ Hz}^{-1}$ ) centered around 100 mHz, but also broad increases to 200 mHz.  
376 Similar observations are made through 23:30 after which VTEC decreases for most PRN

377 with amplitude fluctuations in FFT power  $< 0.02 \text{ TECU}^2 \text{ Hz}^{-1}$  near 100 mHz. During  
378 this time PRN 11 (sea green) crossed the plumes poleward edge, but tracking northward  
379 from inside the plume it observed only slight increases in FFT power beginning near 100  
380 mHz and extending to nearly 400 mHz. This is contrasted with earlier crossings of the  
381 plume's poleward edge that were closer to the tip of the plume and observed much higher  
382 FFT power.

### 3.5. Auroral Observations

383 Figure 7 shows DMSP particle flux intensity at 22:00, 23:00, and 23:20 UT measured  
384 near the observation region. At 22:00 UT DSMP satellite F19 observed increased proton  
385 and electron flux at  $44.4^\circ\text{N}$ ,  $299.8^\circ\text{E}$  geodetic ( $52.4^\circ \text{ N}$ ,  $21.4^\circ \text{ E}$  CGM), suggesting the  
386 auroral boundary was poleward of the SED plume within one hour of the Ann Arbor  
387 observation magnetic local time (MLT). AMPERE summary plots (not shown) also indi-  
388 cate upward radial current beginning at  $\sim 44\text{-}45^\circ\text{N}$  geodetic latitude at Ann Arbor MLT,  
389 further suggesting that electron precipitation, and consequently the equatorward auroral  
390 boundary, began at least several degrees poleward of the SED plume's poleward edge.  
391 Similarly, at 23:00 and 23:17 UT, DMSP satellites F16 and F17 both observed increased  
392 precipitation fluxes beginning at least  $\sim 5^\circ$  latitude poleward of the SED plume. Figure 6  
393 shows the magnetic footprint track for DMSP F17 mapped to 300 km altitude as a white  
394 line with the enhanced particle flux shown from Figure 7 highlighted in pink beginning  
395 near  $\sim 41^\circ\text{N}$ . The period of DMSP precipitation is spatially consistent with the enhanced  
396 TEC observed in bot the single station TEC and MIT Madrigal TEC Maps.

#### 4. Inference of Irregularity Size from Single Station GPS TEC Using Radar Velocities

397 During this same period, both Millstone Hill Incoherent Scatter Radar (ISR) and the  
398 SuperDARN radars at Christmas Valley East, Blackstone, Fort Hays East, and Wallops  
399 Island (e.g., Figure 1) show ion velocities within the Ann Arbor observation area of  $\sim 1000$   
400 ( $\pm 300$ )  $\text{m s}^{-1}$  in the F-region. Assuming the irregularities are frozen-in with the bulk ion  
401 flow, the increased spectral power observed in IPP crossings of the SED/trough and  
402 auroral/trough interfaces is consistent with what would be expected for irregularities  
403 between 3 km ( $\pm 900$  m) and 10 km ( $\pm 3$  km) in size transported past the IPPs at those  
404 velocities. The motion of the IPPs ( $\sim 50 \text{ m s}^{-1}$ ), is nearly stationary relative to the ion  
405 flow and only slightly influence the observed frequency of FFT power ( $\pm 10$  mHz).

#### 5. Discussion

406 During the passage of the SED plume on 17 March 2015 between 20:00 and 23:57 UT  
407 on 17 March 2015, several general trends are observed. First, there is little observed  
408 TEC variation indicated in the FFT spectra equatorward of the advancing SED plume,  
409 along its equatorward edge, or through the plume peak. The equatorward region is best  
410 illustrated by observations from PRNs 3 and 32, which do not cross the SED plume and  
411 travel ahead of the advancing equatorward edge of the plume throughout the observation,  
412 and show only occasional TEC variability — comparable with FFT spectra during quiet-  
413 time conditions. This pattern is further reinforced by similar observations from PRN 16,  
414 as described in Section 3.1, which also travels through the plume system's equatorward  
415 region, but crossing into the plume on a poleward trajectory while showing no FFT power  
416 above  $0.005 \text{ TECU}^2 \text{ Hz}^{-1}$ . During the entire observation, seven PRNs pass through the

417 SED plume and none exhibited FFT power above  $0.005 \text{ TECU}^2 \text{ Hz}^{-1}$  prior to crossing  
418 the plume's poleward gradient. This suggests that small-scale irregularities are scarce  
419 equatorward of the SED plume and and that the plume itself contains few kilometer-  
420 scale irregularities. Second, observations near observations near the plume's poleward  
421 edge exhibit TEC variation and FFT power comparable to that observed in the aurora  
422 ( $\sim 0.1 \text{ TECU}^2 \text{ Hz}^{-1}$ ) — consistent with the variability asymmetry between equatorward  
423 and poleward gradients reported by *Coster* [2007] and *Sun et al.* [2013]. As the PRN  
424 IPPs crossed the poleward edge of the SED plume and its boundary with the trough,  
425 sudden decreases in VTEC were accompanied by rapid fluctuations on multiple scales as  
426 indicated by the VTEC time series and FFT spectra, which showed increased power up to  
427  $0.1 \text{ TECU}^2 \text{ Hz}^{-1}$  between 100 and 300 mHz. Minor TEC fluctuations at similar frequencies  
428 were also found around the edge gradients of the trough minimum, but diminished once  
429 the IPPs had tracked inside it. Importantly, DMSP and AMPERE observations confirm  
430 that GPS TEC variability observed in and around the SED plume was not due to colocated  
431 auroral irregularities. At both 22:00 and 23:00 UT, DMSP indicated vertical proton and  
432 electron fluxes beginning poleward of the SED plume respectively by four degrees latitude  
433 within one hour MLT to the east, and two degrees latitude directly in the observation  
434 area. AMPERE field-aligned-current (FAC) plots at 22:00 (not shown) also indicate  
435 downward FAC extending equatorward to  $\sim 44^\circ$  geographic latitude while the SED plume's  
436 poleward edge was located at  $\sim 42^\circ$ . Finally, as the trough/auroral boundary, an increase  
437 in VTEC variability and the FFT spectra showed increased power  $0.05$  to  $0.1 \text{ TECU}^2 \text{ Hz}^{-1}$   
438 around 100 mHz. This suggests the location of TEC gradients adjacent to the trough and  
439 colocated with high speed ion flow.

440 In their recent paper, *Cherniak and Zakharenkova* [2015] suggest that irregularities  
441 observed in the polar cap may be transported from the mid-latitude SED plume. The  
442 present observation and detection of small-scale irregularities associated with the SED  
443 plume supports this suggestion. Furthermore, observations of longitudinal asymmetries  
444 in TEC structure between PRN with near-simultaneous crossings of the SED plume, such  
445 as those described in sections 3.2 and 3.4 demonstrate that the plume exhibits  $\sim 100$  km  
446 scale longitudinal asymmetries in TEC variability observed at higher latitudes ( $45^\circ$  - $50^\circ$   
447 lat.) that are not observed closer to the SED base region ( $35^\circ$  to  $40^\circ$  lat.). This suggests  
448 that such structuring of the plume may be occurring as the plume moves toward the cusp  
449 and may be an early indicator of the formation of polar patches [*Zou et al.*, 2014].

## 6. Irregularity Altitude

450 Recent work by *Liu et al.* [2016], that characterized the density profile of the SED  
451 plume during 17-March-2015 SED plume suggests that the increased TEC observed in  
452 the SED plume may be due to density enhancements in the topside ionosphere and not  
453 nmF2. This is supported by COSMIC observations that saw a factor of two increase in  
454 topside TEC despite a decrease in nmF2. This suggests that irregularities during this  
455 storm may be occurring higher in altitude than the hmF2, consistent with [*Coster et al.*,  
456 2003] and [*Yuan et al.*, 2009] which found that half of SED TEC is found above 800  
457 km altitude and [*Moldwin et al.*, 2016], which reviewed the body of literature connecting  
458 plasmaspheric and SED plumes and [*Yizengaw*, 2005] which connected the plasmopause  
459 to the mid-latitude trough. This suggests that the irregularities detected in this study may  
460 be generated in the top-side ionosphere or plasmasphere.

## 7. Conclusion

461 Combining temporal and frequency analysis from single GPS ground receivers has been  
462 used to suggest the presence of ionospheric irregularities in various regions of the SED  
463 plume/trough/auroral system as indicated on TEC maps and in the time series data of  
464 single station GPS TEC time series. The addition of radar observations to these analyses  
465 provides an estimate between 3 and 10 km for the irregularity length scales primarily  
466 located on the SED plume's poleward edge, but also observed in the trough for the case  
467 of the 17 March 2015 storm — though this range is limited by the observation sample  
468 rate at 1 Hz. Since smaller irregularities may also be present, future work will investigate  
469 additional storms, expand the range of detectable frequencies with TEC sample rates up  
470 to 20 Hz, and incorporate additional high rate TEC stations now coming online.

### Acknowledgments.

471  
472 This work was supported in part by grants from the National Science Foundation,  
473 AGS-1265651 and AGS-1342968 and the National Aeronautics and Space Administra-  
474 tion, NNX14AF31G. This work was also made possible with data and support from the  
475 CEDAR Archival Madrigal Database at MIT Haystack Observatory, Johns Hopkins Ap-  
476 plied Physics Laboratory and the Defense Meteorological Satellite Program, the AMPERE  
477 team and the AMPERE Science Center, the National Oceanic and Atmospheric Adminis-  
478 tration, the Kyoto Disturbance Storm Time Index, the Blacksburg, Christmas Valley, Fort  
479 Hays, and Wallops Island SuperDARN radar sites, and the Virginia Tech SuperDARN  
480 repository.



481 The authors would also like to acknowledge and thank the following individuals for  
482 review, discussion, and support: Dr. Philip Erickson, Dr. Yu (Jade) Morton, Dr. Anthea  
483 Coster, and Dr. Evan Thomas.

484 University of Michigan GPS TEC Data products are available upon request  
485 (heinet@umich.edu).

486 Madrigal TEC Map Data is available at <http://madrigal.haystack.mit.edu/>.

487 SuperDARN Radar Data is available at <http://vt.superdarn.org/>.

488 DMSP Data can be obtained using the DMSP Tool available at [http://sd-  
www.jhuapl.edu/Aurora/data/app/DMSP.jnlp](http://sd-<br/>489 www.jhuapl.edu/Aurora/data/app/DMSP.jnlp).

## References

- 490 Basu, S., and K. M. Groves (2001), Specification and Forecasting of Outages on Satellite  
491 Communication and Navigation Systems, in *Space Weather*, edited by P. Song, H. J.  
492 Singer, and G. L. Siscoe, pp. 423–430, American Geophysical Union.
- 493 Basu, S., S. Basu, J. J. Makela, E. MacKenzie, P. Doherty, J. W. Wright, F. Rich,  
494 M. J. Keskinen, R. E. Sheehan, and A. J. Coster (2008), Large magnetic storm-induced  
495 nighttime ionospheric flows at midlatitudes and their impacts on GPS-based naviga-  
496 tion systems, *Journal of Geophysical Research: Space Physics*, *113*(A3), A00A06, doi:  
497 10.1029/2008JA013076.
- 498 Bramley, E. N., and R. Browning (1978), Mid-latitude ionospheric scintillation of geosta-  
499 tionary satellite signals at 137 MHz, *Journal of Atmospheric and Terrestrial Physics*,  
500 *40*(12), 1247–1255, doi:10.1016/0021-9169(78)90075-2.

- 501 Cherniak, I., and I. Zakharenkova (2015), Dependence of the high-latitude plasma irreg-  
502 ularities on the auroral activity indices: a case study of 17 March 2015 geomagnetic  
503 storm, *Earth, Planets and Space*, *67*(1), 151, doi:10.1186/s40623-015-0316-x.
- 504 Coster, A., J. Foster, and P. Erickson (2003), Monitoring the ionosphere with GPS, *GPS*  
505 *World*, *14*(5).
- 506 Coster, A. J. (2007), Mitigation of Ionospheric Propagation Errors with GPS, in *2007*  
507 *IEEE Radar Conference*, pp. 922–926, doi:10.1109/RADAR.2007.374342.
- 508 Datta-Barua, S., P. H. Doherty, S. H. Delay, T. Dehel, and J. A. Klobuchar (2003), Iono-  
509 spheric scintillation effects on single and dual frequency GPS positioning, in *Proceedings*  
510 *of ION GPS/GNSS*, pp. 336–346.
- 511 Datta-Barua, S., T. Walter, G. S. Bust, and W. Wanner (2014), Effects of solar cycle 24 ac-  
512 tivity on WAAS navigation, *Space Weather*, *12*(1), 46–63, doi:10.1002/2013SW000982.
- 513 Doherty, P., A. J. Coster, and W. Murtagh (2004), Space weather effects of October–  
514 November 2003, *GPS Solutions*, *8*(4), 267–271, doi:10.1007/s10291-004-0109-3.
- 515 Foster, J. C. (1993), Storm time plasma transport at middle and high latitudes, *Journal*  
516 *of Geophysical Research: Space Physics*, *98*(A2), 1675–1689, doi:10.1029/92JA02032.
- 517 Foster, J. C., and W. J. Burke (2002), SAPS: A new categorization for sub-auroral  
518 electric fields, *Eos, Transactions American Geophysical Union*, *83*(36), 393–394, doi:  
519 10.1029/2002EO000289.
- 520 Foster, J. C., and W. Rideout (2005), Midlatitude TEC enhancements during the October  
521 2003 superstorm, *\grl*, *32*, 12, doi:10.1029/2004GL021719.
- 522 Hargreaves, J. K. (1992), *The solar-terrestrial environment an introduction to geospace–*  
523 *the science of the terrestrial upper atmosphere, ionosphere, and magnetosphere*, Cam-

- 524 bridge University Press, Cambridge [England]; New York, N.Y., oCLC: 852212871.
- 525 Kelley, M. C., M. N. Vlasov, J. C. Foster, and A. J. Coster (2004), A quantitative ex-  
526 planation for the phenomenon known as storm-enhanced density, *Geophysical Research*  
527 *Letters*, *31*(19), L19,809, doi:10.1029/2004GL020875.
- 528 Ledvina, B. M., J. J. Makela, and P. M. Kintner (2002), First observations of intense GPS  
529 L1 amplitude scintillations at midlatitude, *\grl*, *29*, 1659, doi:10.1029/2002GL014770.
- 530 Liu, J., W. Wang, A. Burns, X. Yue, S. Zhang, Y. Zhang, and C. Huang (2016), Profiles  
531 of ionospheric storm-enhanced density during the 17 March 2015 great storm: SED  
532 DURING A GREAT STORM, *Journal of Geophysical Research: Space Physics*, *121*(1),  
533 727–744, doi:10.1002/2015JA021832.
- 534 Love, J. J., and J. Rigler (2015), 17 March 2015.
- 535 Moldwin, M. B., S. Zou, and T. Heine (2016), The story of plumes: the development of a  
536 new conceptual framework for understanding magnetosphere and ionosphere coupling,  
537 *Annales Geophysicae*, *34*(12), 1243–1253, doi:10.5194/angeo-34-1243-2016.
- 538 Pi, X., A. J. Mannucci, U. J. Lindqwister, and C. M. Ho (1997), Monitoring of global iono-  
539 spheric irregularities using the Worldwide GPS Network, *Geophysical Research Letters*,  
540 *24*(18), 2283–2286, doi:10.1029/97GL02273.
- 541 Schunk, R., and A. Nagy (2009), *Ionospheres: Physics, Plasma Physics, and Chemistry*,  
542 Cambridge University Press, Cambridge.
- 543 Seo, J., T. Walter, and P. Enge (2011), Correlation of GPS signal fades due to ionospheric  
544 scintillation for aviation applications, *Advances in Space Research*, *47*(10), 1777–1788,  
545 doi:10.1016/j.asr.2010.07.014.

- 546 Simon, A. (1963), Instability of a Partially Ionized Plasma in Crossed Electric and Mag-  
547 netic Fields, *Physics of Fluids (1958-1988)*, 6(3), 382–388, doi:10.1063/1.1706743.
- 548 Sun, Y.-Y., T. Matsuo, E. A. Araujo-Pradere, and J.-Y. Liu (2013), Ground-based GPS  
549 observation of SED-associated irregularities over CONUS: SED-ASSOCIATED IRREG-  
550 ULARITIES OVER CONUS, *Journal of Geophysical Research: Space Physics*, 118(5),  
551 2478–2489, doi:10.1029/2012JA018103.
- 552 van der Meeren, C., K. Oksavik, D. Lorentzen, J. I. Moen, and V. Romano (2014), GPS  
553 scintillation and irregularities at the front of an ionization tongue in the nightside polar  
554 ionosphere, *Journal of Geophysical Research: Space Physics*, 119(10), 8624–8636, doi:  
555 10.1002/2014JA020114.
- 556 Yeh, K. C., and C.-H. Liu (1982), Radio wave scintillations in the ionosphere, *Proceedings*  
557 *of the IEEE*, 70(4), 324–360.
- 558 Yizengaw, E. (2005), The altitude extension of the mid-latitude trough and its  
559 correlation with plasmopause position, *Geophysical Research Letters*, 32(9), doi:  
560 10.1029/2005GL022854.
- 561 Yuan, Z.-G., X.-H. Deng, S.-R. Zhang, W.-X. Wan, and B. W. Reinisch (2009), F region  
562 behavior in the SED plume during a geomagnetic superstorm: A case study, *Journal of*  
563 *Geophysical Research (Space Physics)*, 114, 8303, doi:10.1029/2008JA013841.
- 564 Zou, S., A. J. Ridley, M. B. Moldwin, M. J. Nicolls, A. J. Coster, E. G. Thomas, and  
565 J. M. Ruohoniemi (2013), Multi-instrument observations of SED during 24-25 October  
566 2011 storm: Implications for SED formation processes, *Journal of Geophysical Research*  
567 *(Space Physics)*, 118, 7798–7809, doi:10.1002/2013JA018860.

568 Zou, S., M. B. Moldwin, A. J. Ridley, M. J. Nicolls, A. J. Coster, E. G. Thomas, and  
569 J. M. Ruohoniemi (2014), On the Generation/Decay of the Storm-Enhanced Density  
570 (SED) Plumes: Role of the Convection Flow and Field-Aligned Ion Flow, *Journal of*  
571 *Geophysical Research: Space Physics*, p. 2014JA020408, doi:10.1002/2014JA020408.

Author Manuscript

D R A F T

March 11, 2017, 1:12pm

D R A F T

**Figure 1.** The SED plume is visible in the  $1^\circ \times 1^\circ$  TEC map as a red band stretching toward the northwest at 22:00 UT. The colored circles indicate the location of SuperDARN Radar backscatter and line-of-site ion speeds from Christmas Valley East, Fort Hays East and Wallops Island while the polar equipotential lines (solid lines) show the direction of plasma convection (westward within the Great Lakes region). The day/night terminator is shown as a dotted line. *Figure courtesy of Evan Thomas, Virginia Technological University.*

**Figure 2.** *Top:* Frequency and phase response of high pass filter used to remove low frequency ( $<100$  mHz, long temporal) background from the STEC signal. *Bottom:* The unfiltered STEC signal from PRN 23 is shown in blue while the filtered signal is shown in orange. The filter removed the large-scale STEC variations associated with the SED plume in order to extract smaller-scale variations of interest to this study



**Figure 3.** *Left:* Interpolated Madrigal VTEC map with 5-minute IPP tracks for the interval ending at 20:45 UT. The location of the ANNA receiver is marked with a five-pointed star and a white circle demarcates the field-of-view boundary with a 20° elevation mask. The SED plume, SED base region, and mid-latitude trough are visible. *Inset:* TEC over North America. *Right Top:* The cumulative VTEC time series from 20:00. The five-minute FFT window is indicated by the two black vertical lines at the end of the time series. *Right Bottom:* The 5-minute FFT for the observable GPS PRN.

D R A F T

March 11, 2017, 1:12pm

D R A F T



**Figure 4.** *Left:* Interpolated Madrigal VTEC map with 5-minute IPP tracks for the interval ending at 22:00 UT. The location of the ANNA receiver is marked with a five-pointed star and a white circle demarcates the field-of-view boundary with a 20° elevation mask. The SED base region, SED plume, mid-latitude trough, and auroral enhancement are visible from bottom to top. *Inset:* TEC over North America. *Right Top:* The cumulative VTEC time series from 20:00. The five-minute FFT window is indicated by the two black vertical lines at the end of the time series. *Right Bottom:* The





**Figure 5.** *Left:* Interpolated Madrigal VTEC map with 5-minute IPP tracks for the interval ending at 23:05 UT. The SED base region, SED plume, mid-latitude trough, and auroral enhancement are visible from bottom to top with all IPP tracks (with the exception of PRN 23) are located in the mid-latitude trough. *Inset:* TEC over North America. *Right Top:* The cumulative VTEC time series from 21:00. *Right Bottom:* The 5-minute FFT for the observable GPS PRN.



**Figure 6.** *Left:* Interpolated Madrigal VTEC map with 5-minute IPP tracks for the interval ending at 23:205 UT. The SED plume, SAPS, trough, and auroral enhancement are visible from bottom to top and all of the IPP tracks (except PRN 23) are located within the auroral zone. The magnetic footprint track for DMSF F17 mapped to 300 km altitude (white line) is also shown with the detected enhanced particle precipitation (shown in Figure 7) flux highlighted in magenta along the track beginning near  $\sim 41^\circ\text{N}$ .

*Inset:* TEC over North America. *Right Top:* The cumulative VTEC time series from

23:25 to 23:45. *Right Bottom:* The 5-minute STECF for the observable GPS PRN.

D R A F T

F19\_ParticlePrecip\_076\_2202-2209UT.pdf

F16\_ParticlePrecip\_076\_2300-2306UT.pdf

F17\_ParticlePrecip\_076\_2316-2322UT.pdf

D R A F T

March 11, 2017, 1:12pm

D R A F T

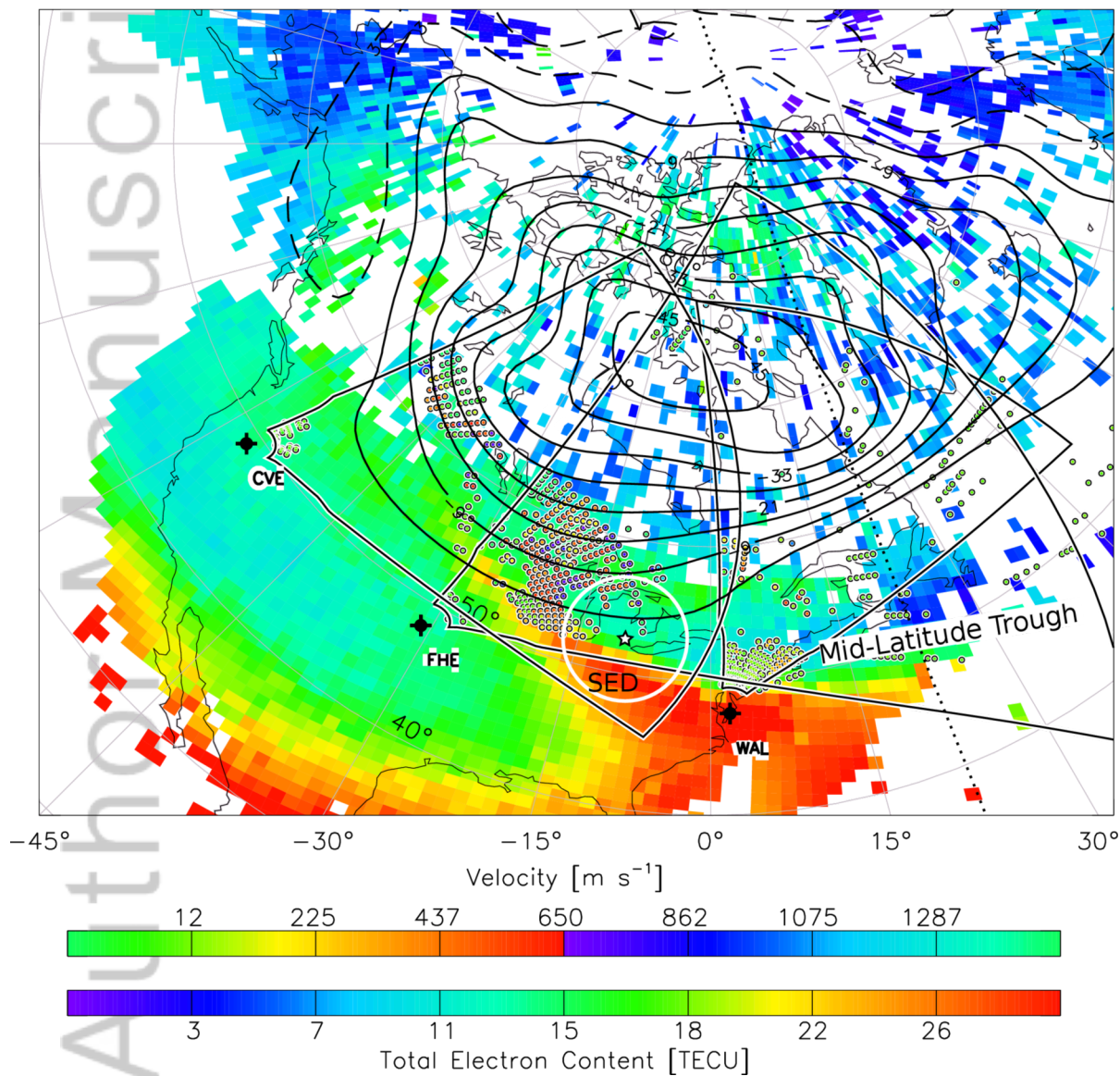
**Figure 7.** *Top:* DMSP F19 particle flux

showing auroral electron precipitation was

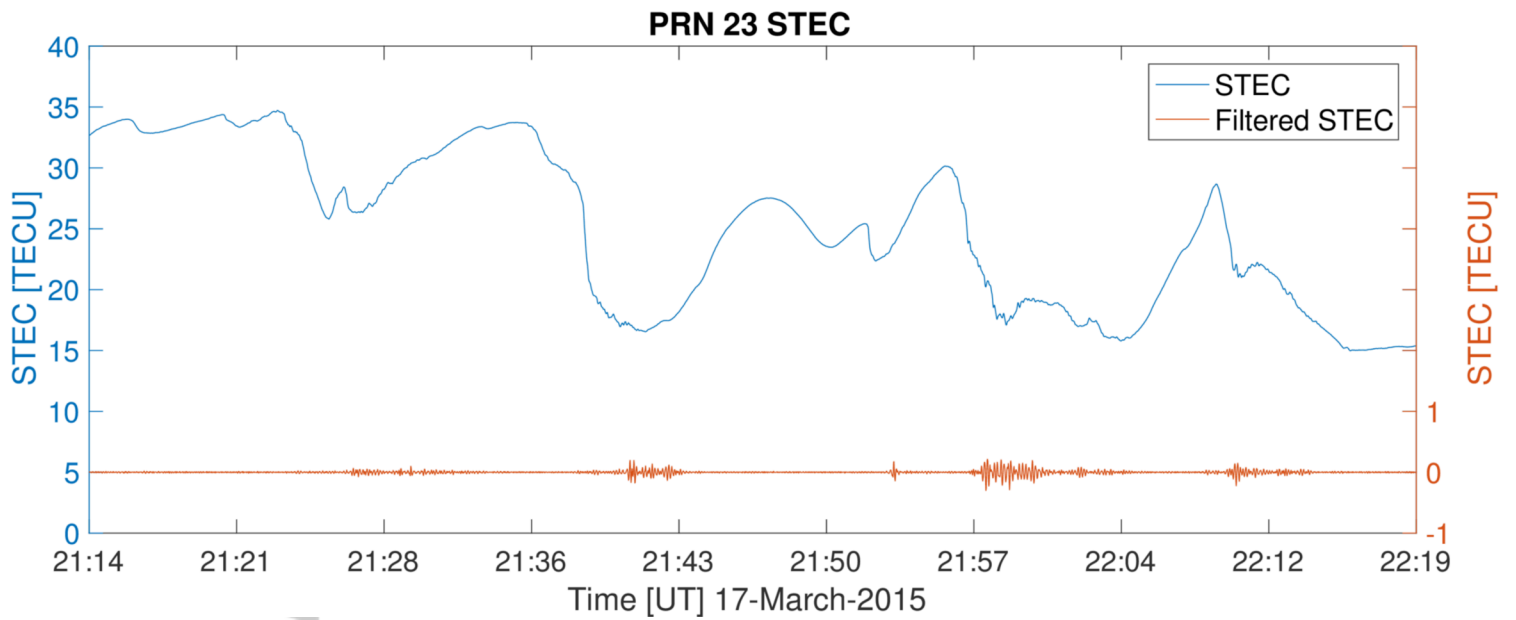
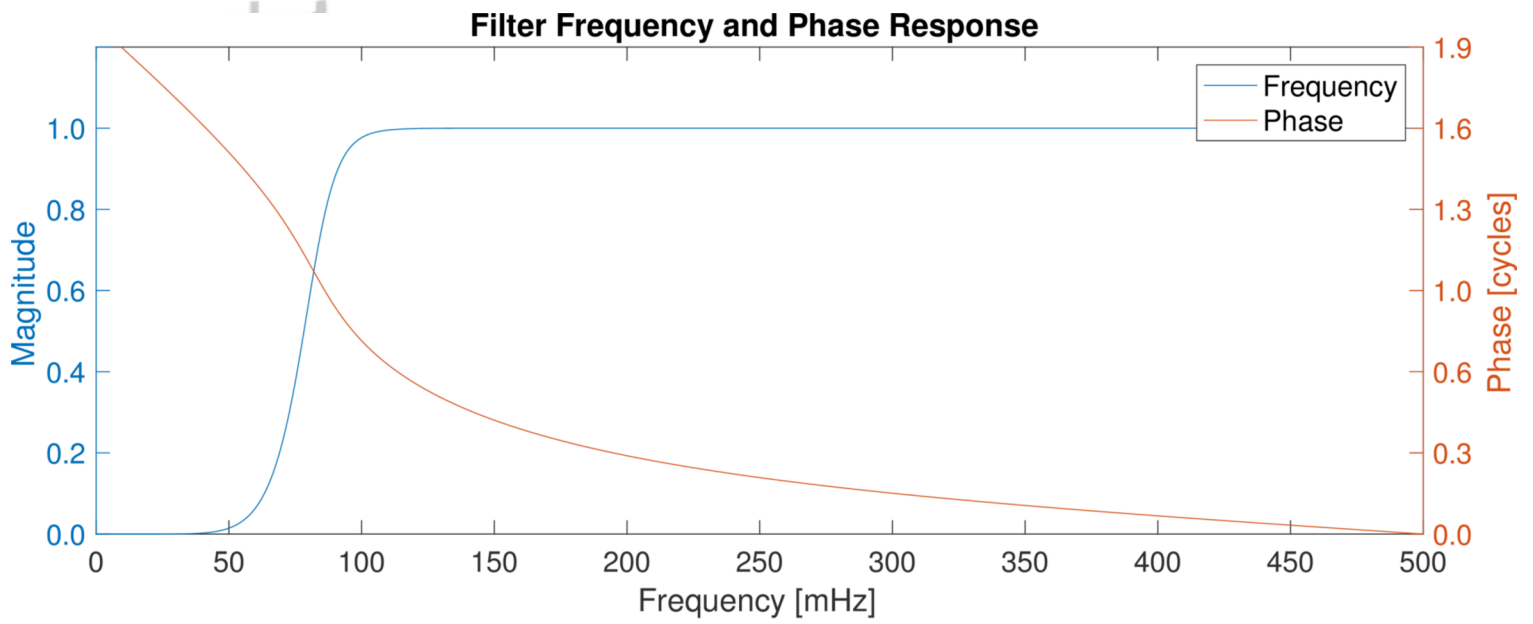
4° poleward of the SED plume within 18°

This article is protected by copyright. All rights reserved.

TOTAL ELECTRON CONTENT 17/Mar/2015 22:00:00.0  
GPS Receiver Network (Millstone Hill) to  
17/Mar/2015 22:05:00.0



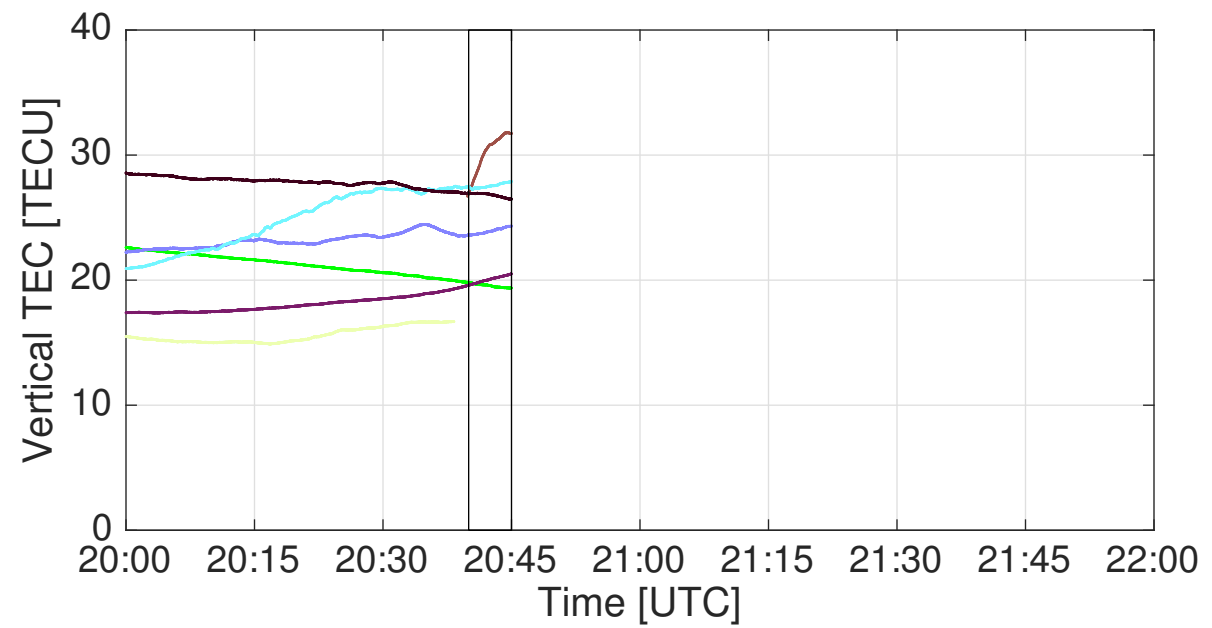
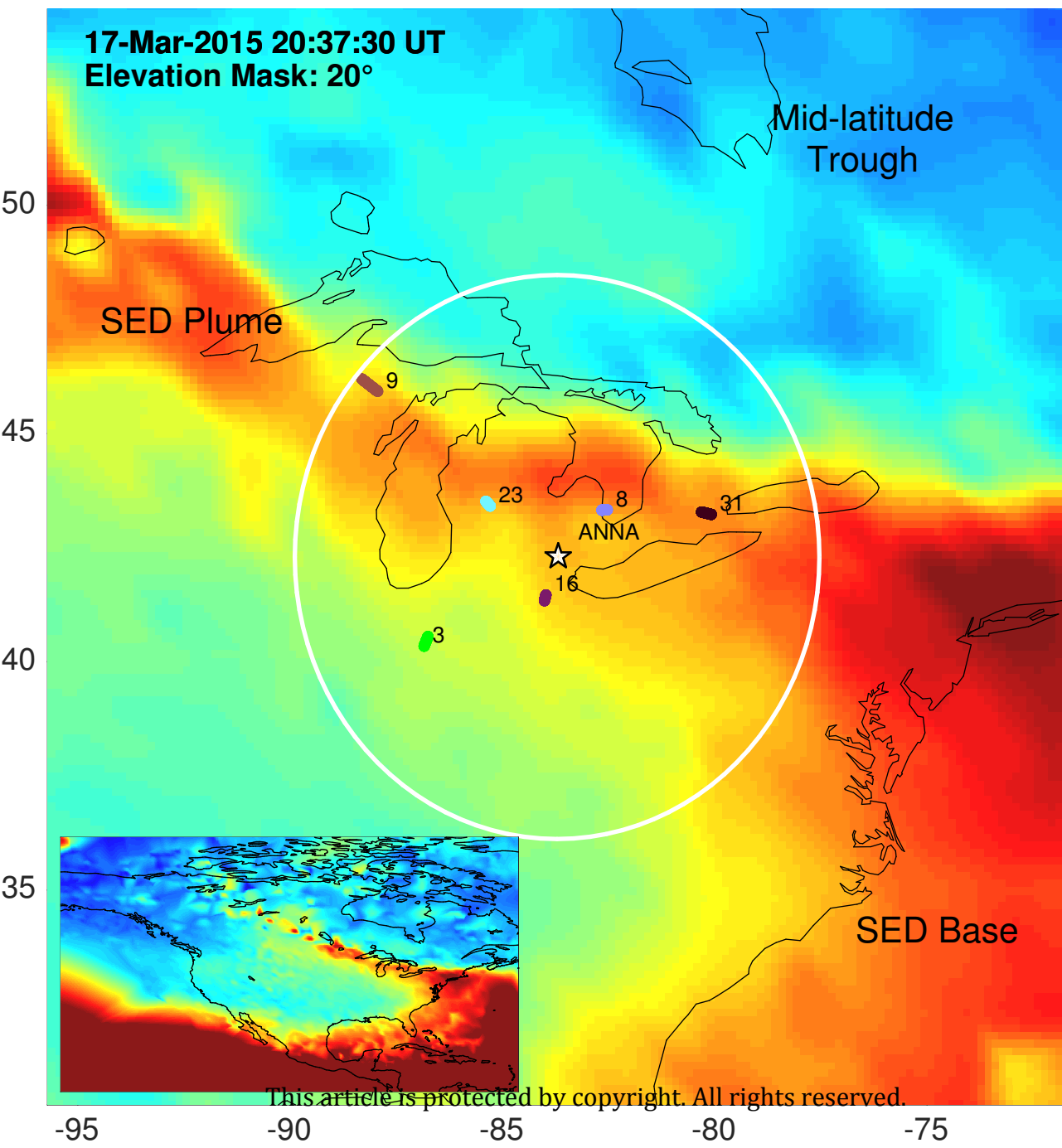
2016ja022965-f01-z-eps



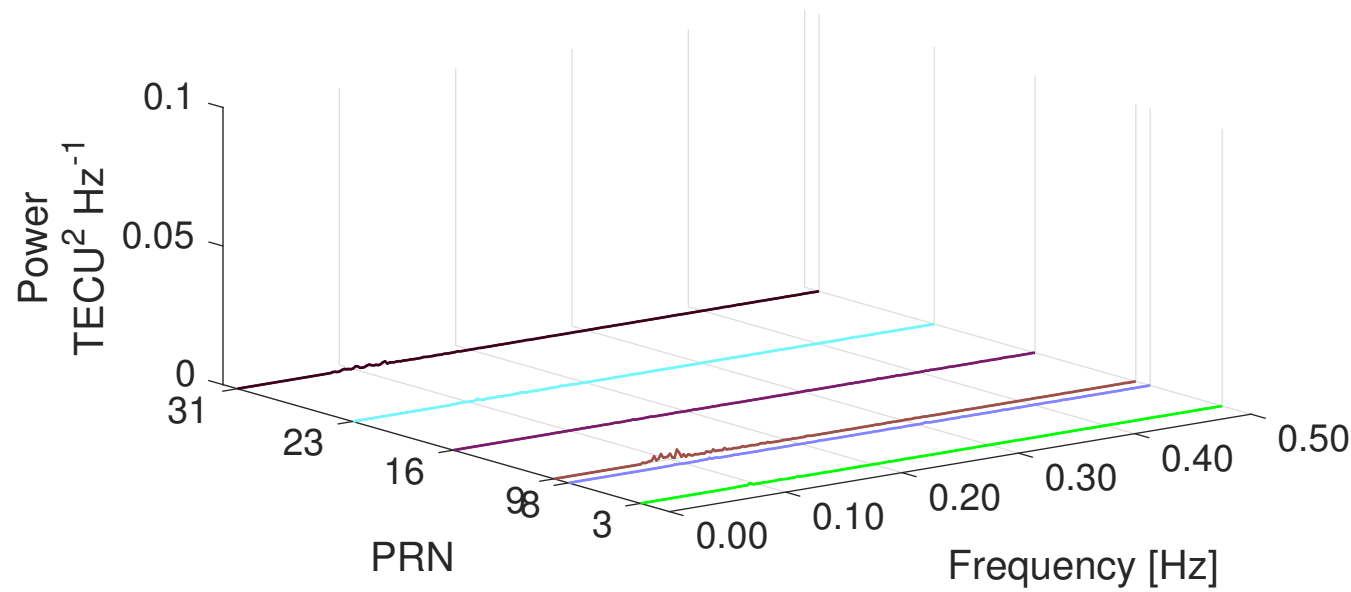
2016ja022965-f02-z-.eps

# TEC Observations from ANNA: 42.2945 N -83.7116 E

17-Mar-2015 20:37:30 UT  
Elevation Mask: 20°

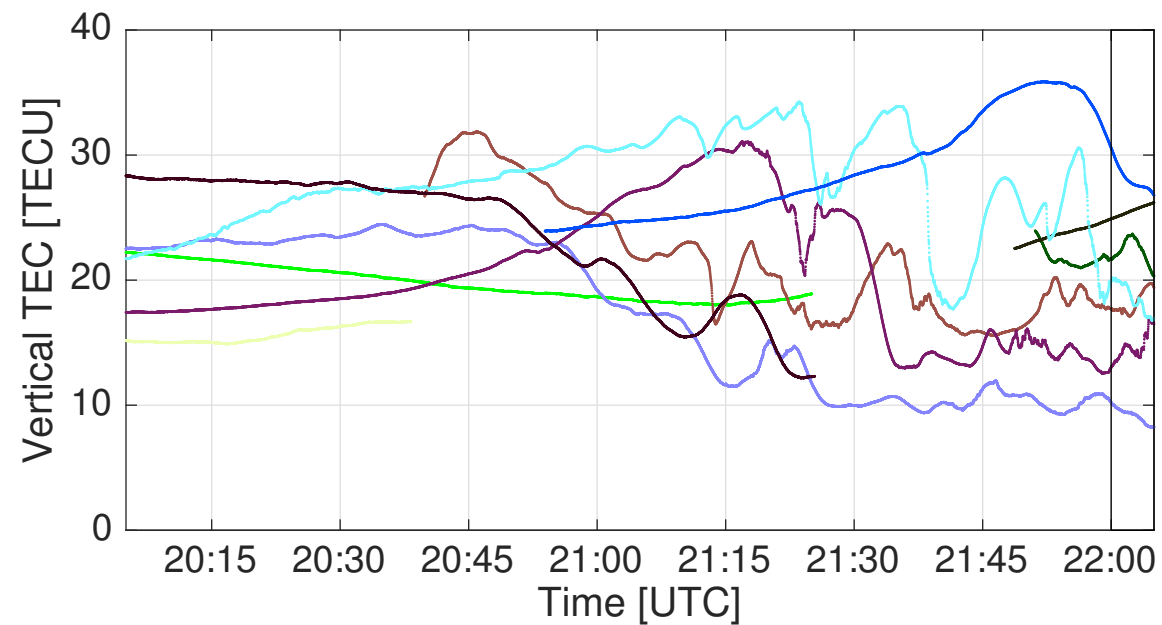
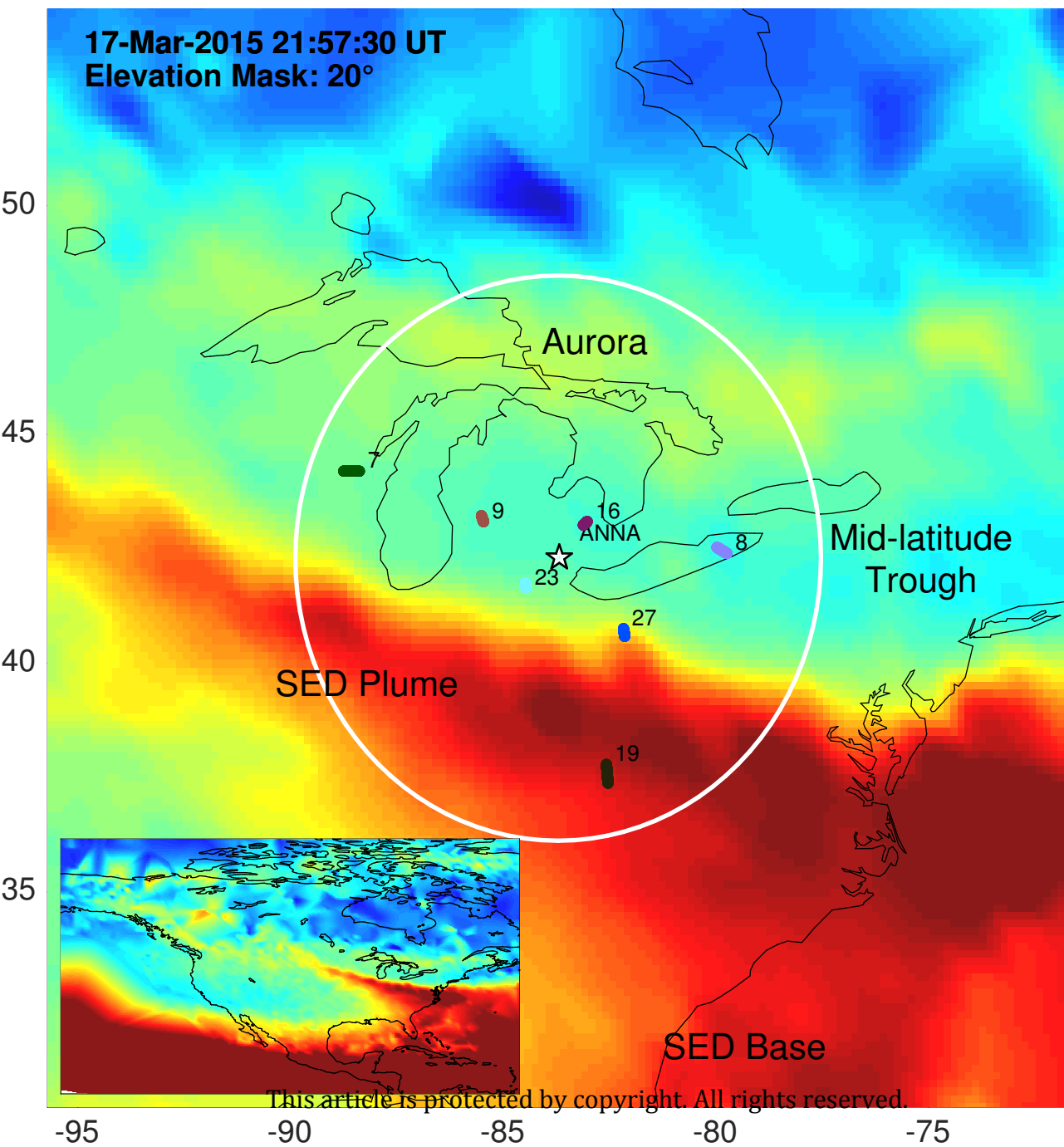


**FFT Power Spectrum STEC  
20:40:00-20:45:00**

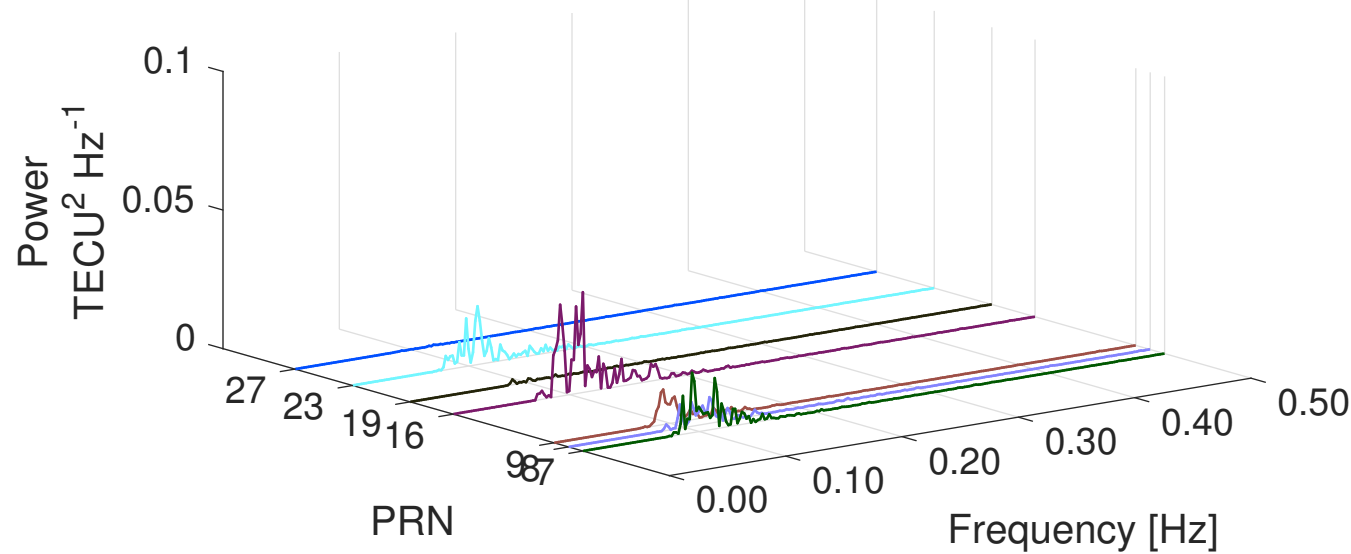


# TEC Observations from ANNA: 42.2945 N -83.7116 E

17-Mar-2015 21:57:30 UT  
Elevation Mask: 20°

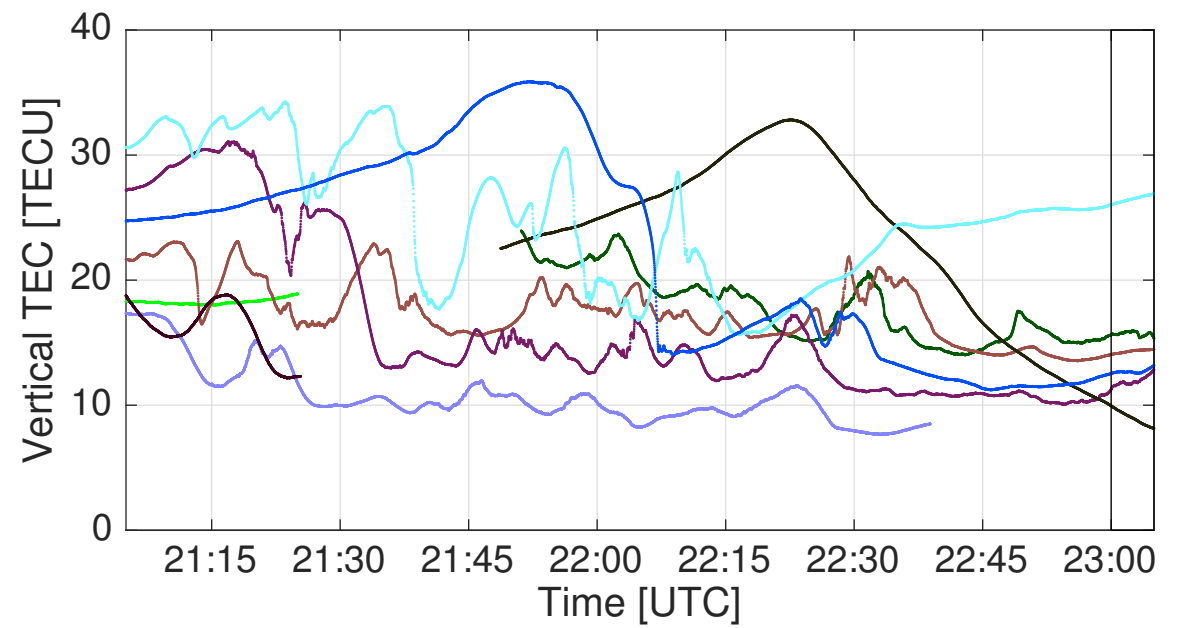
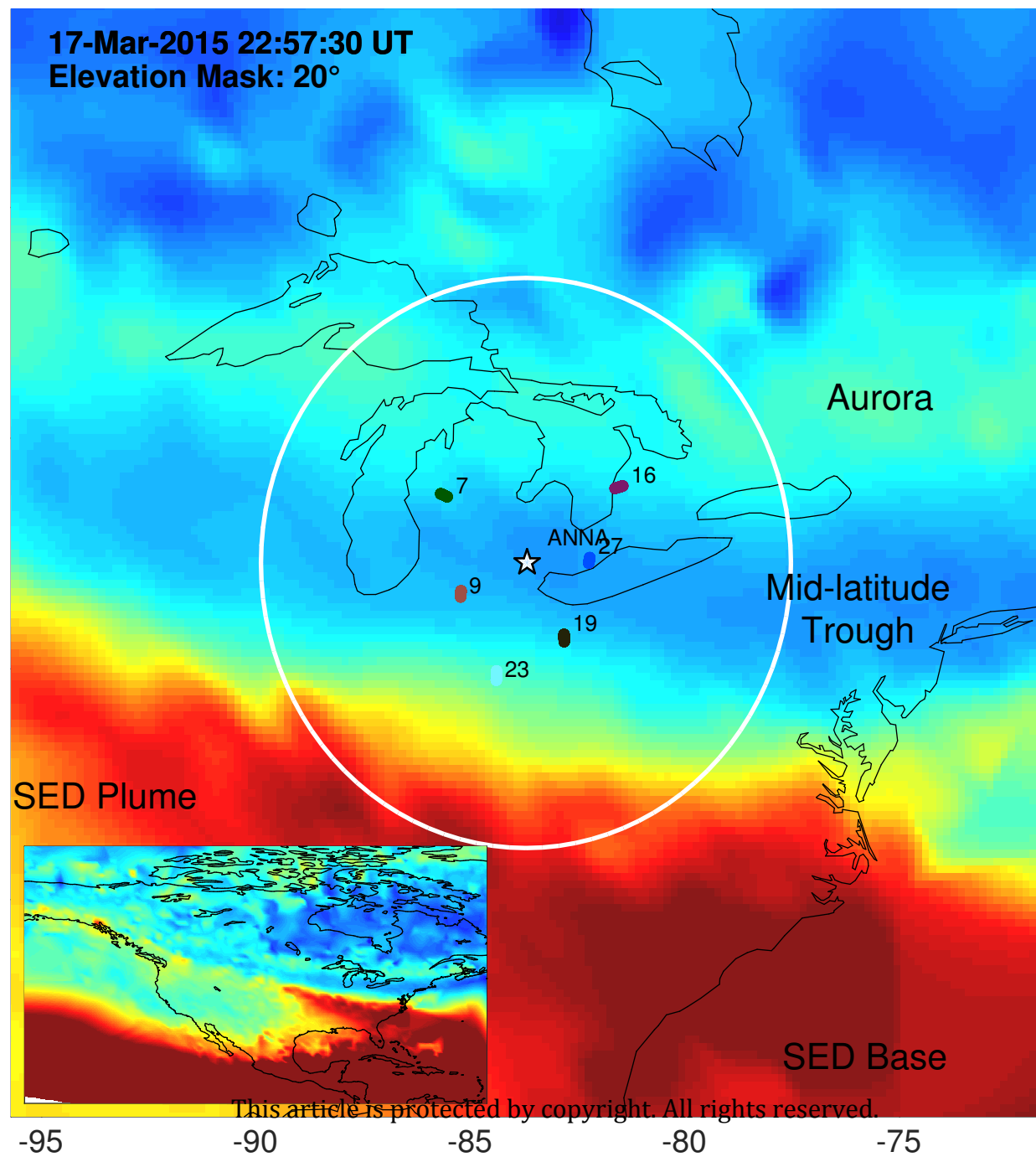


## FFT Power Spectrum STEC 22:00:00-22:05:00

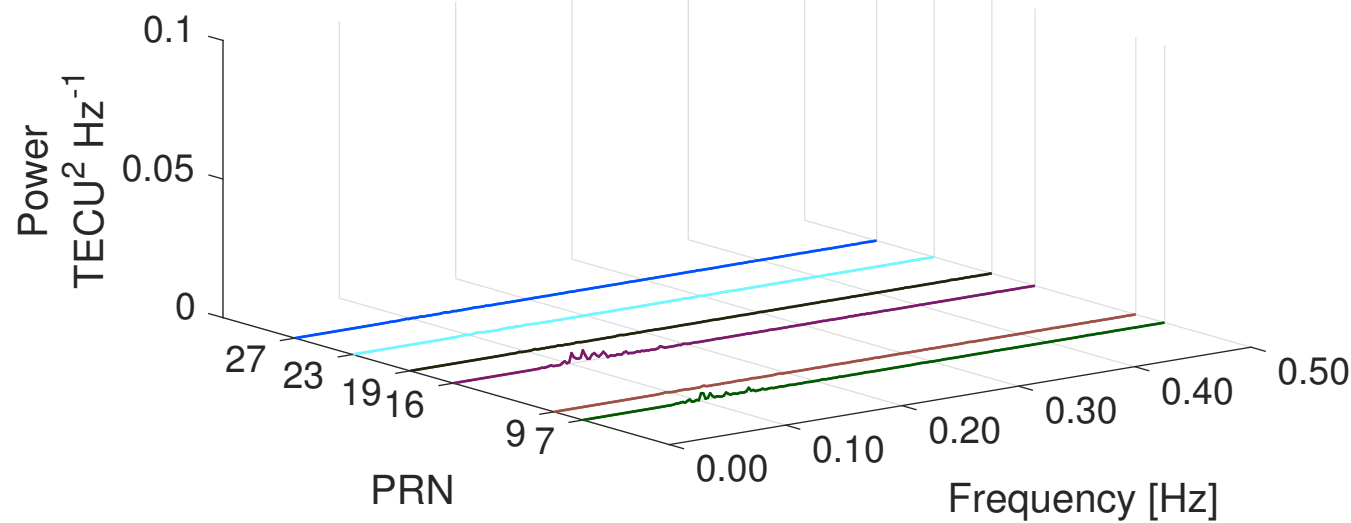


# TEC Observations from ANNA: 42.2945 N -83.7116 E

17-Mar-2015 22:57:30 UT  
Elevation Mask: 20°



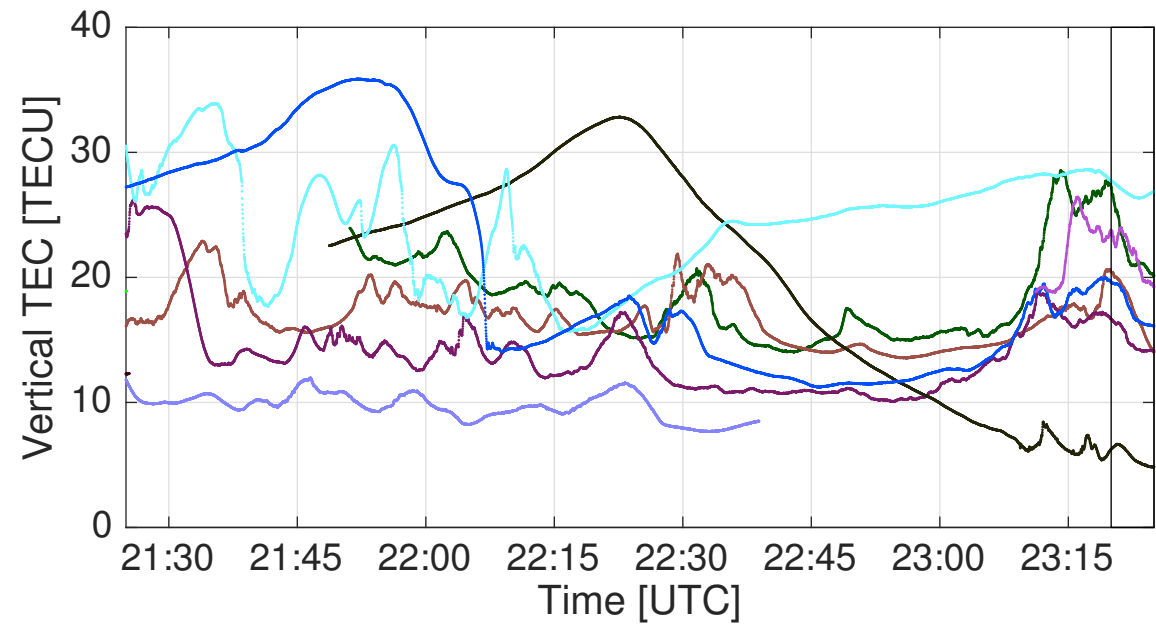
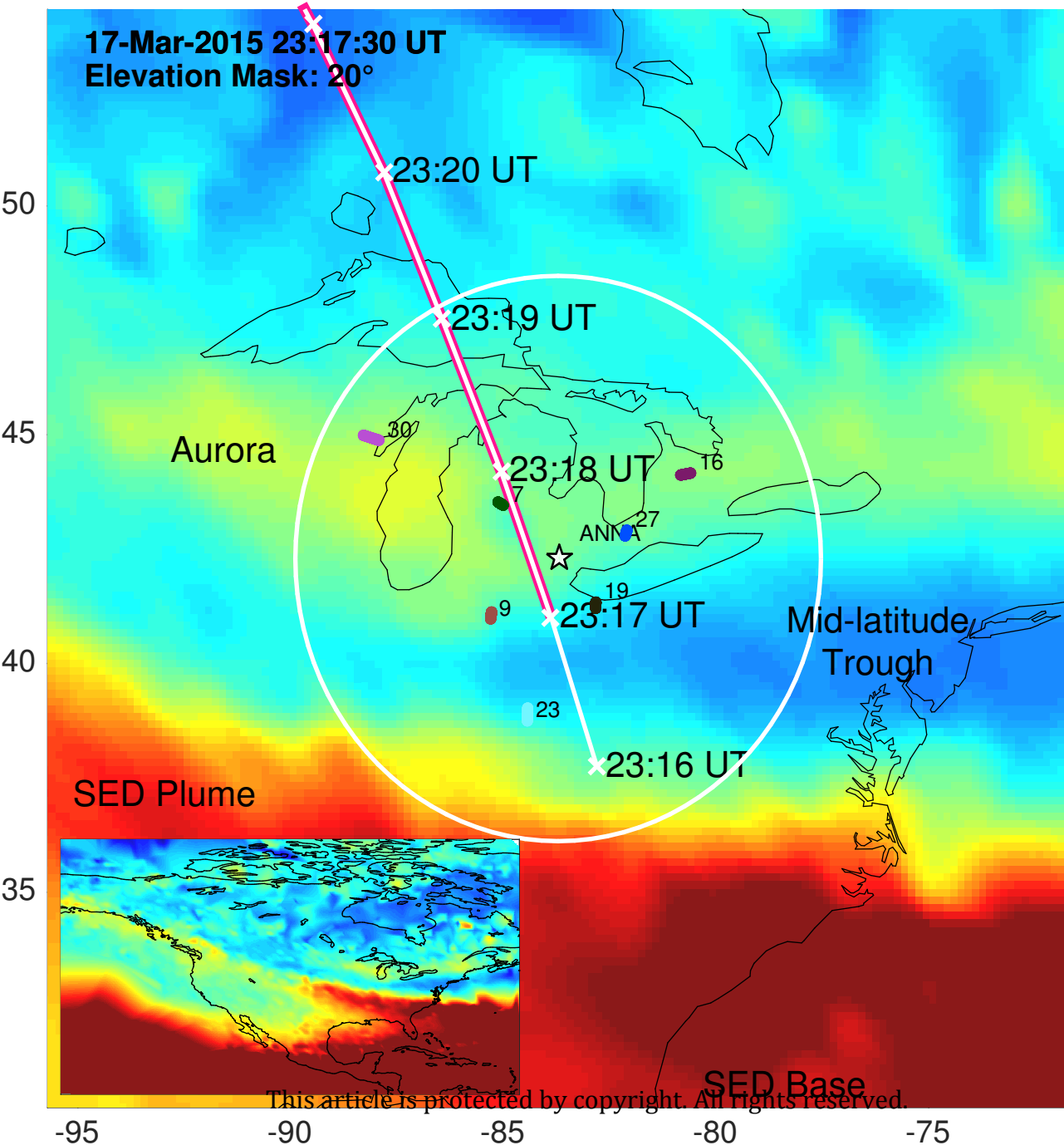
**FFT Power Spectrum STEC**  
**23:00:00-23:05:00**



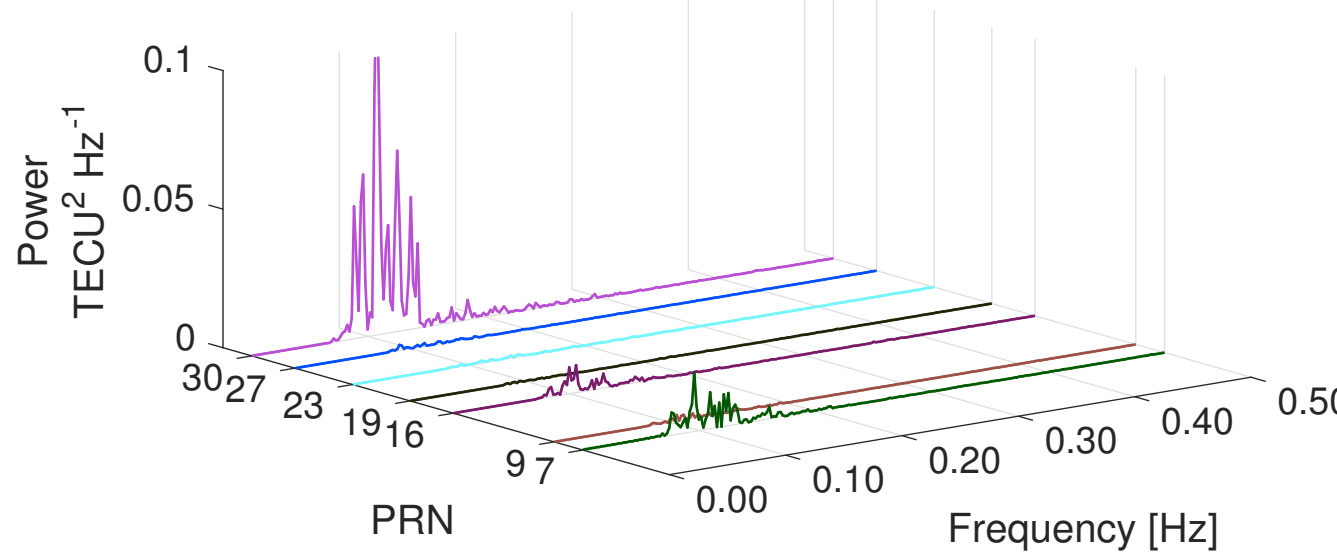


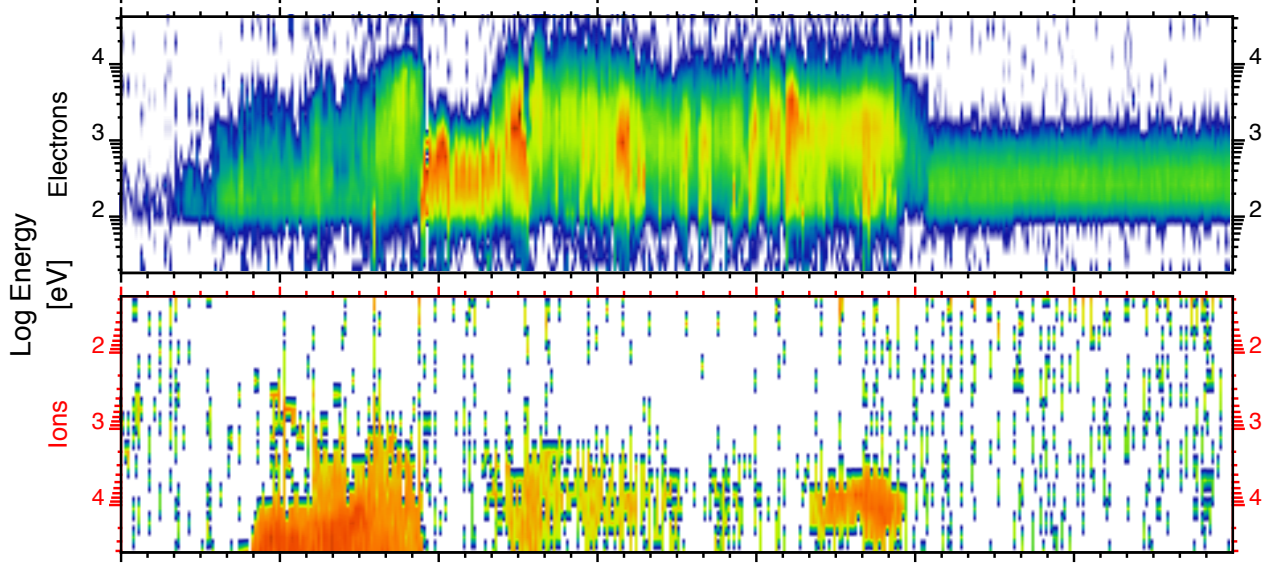
# TEC Observations from ANNA: 42.2945 N -83.7116 E

17-Mar-2015 23:17:30 UT  
Elevation Mask: 20°

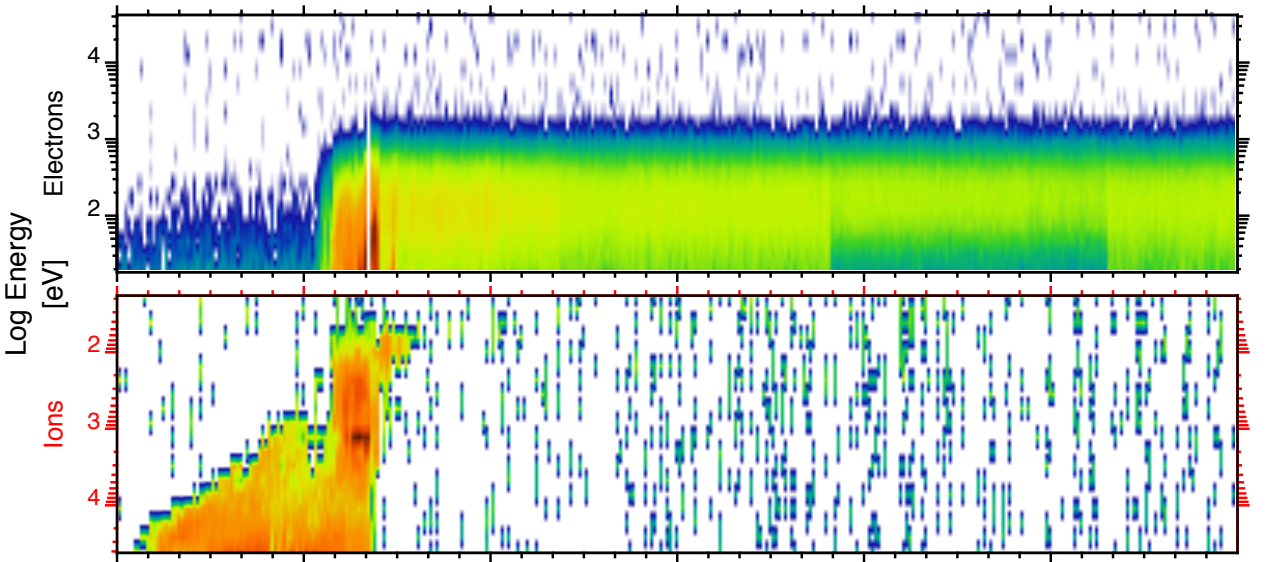


**FFT Power Spectrum STEC**  
23:20:00-23:25:00

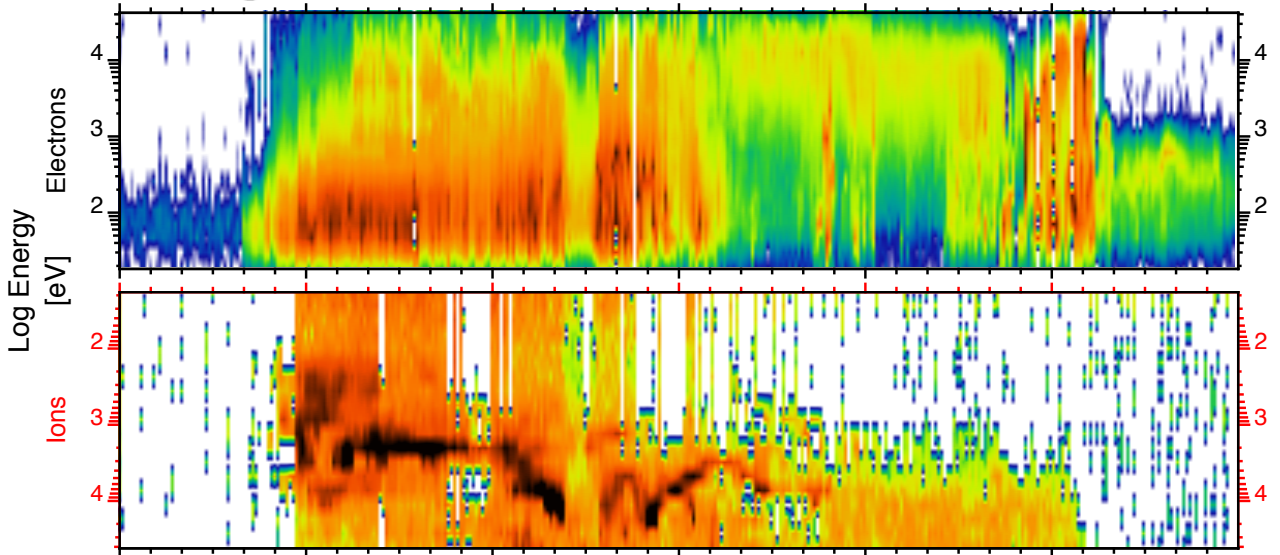




UT	22:02:00	22:03	22:04	22:05	22:06	22:07	22:08	22:09:00
LAT	43.1	46.6	50.0	53.4	56.9	60.2	63.6	66.9
LON	300.4	299.0	297.5	295.9	293.9	291.7	289.0	285.6
MLAT	53.4	56.8	60.2	63.6	67.0	70.3	73.6	76.7
MLT	18:16	18:11	18:06	17:59	17:52	17:41	17:28	17:09



UT	23:00:00	23:01	23:02	23:03	23:04	23:05	23:06:00
LAT	44.5	48.0	51.4	54.8	58.2	61.6	64.9
LON	254.5	253.1	251.6	249.9	247.9	245.5	242.6
MLAT	55.7	58.6	61.5	64.3	67.1	69.7	72.1
MLT	15:07	14:58	14:47	14:34	14:18	13:60	13:36



UT	23:16:00	23:17	23:18	23:19	23:20	23:21	23:22:00
LAT	35.9	39.4	42.8	46.3	49.7	53.1	56.5
LON	277.4	276.3	275.1	273.7	272.3	270.6	268.7
MLAT	49.9	52.9	55.9	58.9	62.0	64.9	67.9
MLT	17:11	17:06	16:59	16:52	16:43	16:32	16:20

JHU/APL

